UNIVERSITY OF CALIFORNIA SAN DIEGO

Implications of Systemic Hematocrit and the Endothelial Glycocalyx Layer on Microvascular Hemodynamics

A Thesis submitted in partial satisfaction of the
requirements for the degree
Master of Science

in

Bioengineering

by

Vivek P. Jani

Committee in charge:

Professor Pedro Cabrales, Chair
Professor Marcos Intaglietta
Professor Kevin King

2018

The Thesis of Vivek P. Jani is approved, and it is acceptable in quality and form for publication on microfilm and electronically:

_____

_____

_____

Chair

University of California San Diego

2018

DEDICATION

To my parents, Pinakin and Chetna Jani,

without whom I would not be where I am today.

EPIGRAPH

Engineering is quite different from science.

Scientists try to understand nature.

Engineers try to make things that do not exist in nature.

—Professor Y.C. Fung

TABLE OF CONTENTS

LIST OF FIGURES

LIST OF TABLES

ACKNOWLEDGEMENTS

I would like to acknowledge Professor Pedro Cabrales for his support as the chair of my committee. Throughout the years, Professor Cabrales has been an invaluable mentor, and his guidance has ignited a passion for engineering and research that has lead me to pursue a career as a physician scientist.

I would like also like to acknowledge Cynthia Walser for preparation of all animals and for being an invaluable mentor and colleague in the lab. I would also like to thanks Alexander T. Williams and all other students in the Cabrales Lab for their continued guidance and support.

Chapter 1, in full, is a reprint of the material as it appears in Implications Enzymatic Degradation of the Endothelial Glycocalyx on the Microvascular Hemodynamics and the Arteriolar Red Cell Free Layer of the Rat Cremaster Muscle 2018. Yalcin, O., Jani, V. P., Johnson, P. C., & Cabrales, P. Frontiers in Physiology, 9, 168. http://doi.org/10.3389/fphys.2018.00168. The thesis author was the primary investigator and author of this paper.

Chapter 2, in full, is currently being prepared for submission for publication of the material as it appears in Implications of Systemic Hematocrit on Microvascular Hemodynamics, From Blood Flow to the Radial Distribution of Red Cells and Plasma in Microvessels 2018. Jani, V. P., Yalcin, O., Lucas, A., Williams, A. T., Johnson, P. C., & Cabrales, P. The thesis author was the primary investigator and author of this material.

VITA

2017	B. S. in Bioengineering *summa cum laude*, University of California San Diego
2017	B. S. in Human Biology *summa cum laude*, University of California San Diego
2017-2018	Graduate Teaching Assistant, University of California San Diego
2018	M. S. in Bioengineering, University of California San Diego

PUBLICATIONS

Jani, V. P., Yalcin, O., Williams, A. T., Popovsky, M. A., & Cabrales, P. (2017). Rat red blood cell storage lesions in various additive solutions. *Clinical Hemorheology and Microcirculation*, 67(1), 4557.

Jani, V., Ingulli, E., Mekeel, K., & Morris, G. P. (2017). Root cause analysis of limitations of virtual crossmatch for kidney allocation to highly-sensitized patients. *Human Immunology*, 78(2), 7279.

Ao-ieong, E. S. Y., Williams, A., Jani, V., & Cabrales, P. (2017). Cardiac function during resuscitation from hemorrhagic shock with polymerized bovine hemoglobin-based oxygen therapeutic. *Artificial Cells, Nanomedicine, and Biotechnology*, 45(4), 686693.

Jani, V. P., Jelvani, A., Moges, S., Nacharaju, P., Roche, C., Dantsker, D., Cabrales, P. (2017). Polyethylene Glycol Camouflaged Earthworm Hemoglobin. *PLOS ONE*, 12(1), e0170041.

Yalcin, O., Jani, V. P., Johnson, P. C., & Cabrales, P. (2018). Implications Enzymatic Degradation of the Endothelial Glycocalyx on the Microvascular Hemodynamics and the Arteriolar Red Cell Free Layer of the Rat Cremaster Muscle. *Frontiers in Physiology*, 9, 168.

ABSTRACT OF THE THESIS

Implications of Systemic Hematocrit and the Endothelial Glycocalyx Layer on Microvascular Hemodynamics

by

Vivek P. Jani

Master of Science in Bioengineering

University of California San Diego, 2018

Professor Pedro Cabrales, Chair

The microcirculation consists of blood vessels smaller than 40 μm, namely arterioles, venuoles, and capillaries. Microvessels prove to be the primary location of oxygen delivery and transport in the circulation, and their analysis has many implications in the understanding and development of human disease. While the role of the microcirculation has been understated in the past, recent research has alluded to its increasing clinical relevance. The objective of this thesis is to provide insight into both the physiology and microvascular hemodynamics of the microcirculation by presenting in vivo data of well-known microcirculatory phenomena. The first chapter of this thesis presents a published study on the effects of the endothelial glycocalyx layer

(EGL), a complex layer of proteoglycans and glycoproteins, on microvascular hemodynamics via its enzymatic degradation. The second chapter of this thesis presents work investigating the effects of systemic hematocrit on microvascular hemodynamics, particularly the effects of hemoconcentration and hemodilution on blood flow and the thickness of the arteriolar cell free layer. The final chapter of this thesis presents improved computer vision and image processing techniques developed to analyze the spatial variations in the arteriolar cell free layer within a single vessel. The data presented in this thesis, in addition to presenting experimental evidence for well-known microcirculatory phenomena observed *in vivo*, provide insight into the implications of microvascular hemodynamics in human disease.

Introduction

The microcirculation consists of blood vessels smaller than 40 μm, namely arterioles, venuoles, and capillaries. Microvessels prove to be the primary location of oxygen delivery and transport in the circulation, and their analysis has many implications in the understanding and development of human disease [1]. Research of the microcirculation broadly consists of understanding the role of microcirculatory dysfunction in the development of human disease and utilizing the physiology of transport in the microcirculation to understand transfusion and develop blood substitutes, namely Hemoglobin Based Oxygen Carriers (HBOCs) [1, 2]. Pathophysiological changes in the microcirculation have been implicated in diagnosing pre-hypertension, pre-diabetes, and pre-sepsis [3, 4]. Furthermore, recent research has demonstrated that patients with congestive heart failure and diabetes are more susceptible to recurrent heart failure related hospitalizations, primarily due to microvascular damage induced by diabetes [3]. While the role of the microcirculation has been understated in the past, recent research has alluded to its increasing clinical relevance.

The biomechanics and transport phenomena associated with the microcirculation have been an area of research interest for many years and are well understood [1]. Much work has been done to understand changes in hemodynamics as a function of vessel size, hematocrit, erythrocyte rigidity, and leukocyte activation [1, 5]. Beginning with the work of Fahraeus in 1929 and the discovery of both the Fahreaus and Fahraeus-Lindqvuist effects, it has been well known that the non-Newtonian properties of blood have physiological significance in the circulation [6, 7]. Three different flow regimes are known to exist in the circulation: (1) pipe flow in microvessels with diameters between 20 and 100 μm, (2) plug, or bolus, flow in capillaries with diameters less than 10 μm, and (3) a combination of plug and pipe flow in larger vessels due the formation of the Rouleaux stacks along the centerline [1]. Much of this work has been mathematically quantified utilizing Cassons equation and more complex solutions of Navier Stokes under the assumption of dynamic viscous flow. More significant, however, is the physiological understanding of

perfusion that resulted from such analyses [1]. The complex non-linearities in microvascular blood flow function to minimize flow resistance and apparent viscosity *in vivo*, minimizing energy expenditure while maximizing oxygen delivery. Deviations from baseline fluid forces can be sensed by the microvasculature via the shear stresses exerted on endothelial cells lining the lumen of the vasculature. Consequently, changes in perfusion and blood flow can be induced via endogenous pathways in the microcirculation, including Nitric Oxide (NO) induced vasodilation [8].

One interesting phenomenon that results from the non-linear rheological properties of blood in the microcirculation is the formation of a cell free layer (CFL), or lubrication layer [9]. The deformability of RBCs allow them to pass through capillaries much smaller than their characteristic size, giving rise to complex, nonlinear blood rheological properties. Consequently, blood flow in microcirculatory vessels is defined by complex two-phase flow paradigms, in which blood flow is characteristically defined by a central, solid core of packed RBCs and a RBC depleted zone near the vessel wall, known as the RBC Cell Free Layer (CFL). The formation of the CFL in flowing blood is an important hemodynamic feature of the blood flow in the microcirculation, since it corresponds to a low viscosity zone, which acts as a lubricating hydrodynamic layer, reducing resistance to flow between the RBC core and the vessel wall [9]. Furthermore, the thickness of the CFL is proportional to the yield stress of the flowing fluid and depends on the hematocrit (Hct), RBC aggregation, vessel geometry, the migration forces driving the RBCs to away from the vessel wall, and the endothelial glycocalyx [10]. The objective of this thesis, in part, is to identify the physiological relevance of both the CFL and the endothelial glycocalyx layer and their relevance in various hematological and cardiovascular pathophysiologies.

In addition to the research of the biomechanics and rheological properties of blood and its implications on the physiology of the microcirculation, oxygen delivery and fluid transport between the tissue and microvessels has been a significant area of research. In large part, this is

due to the fact that, clinically, quantification of tissue oxygen concentration as opposed to blood oxygen saturation is a more useful metric of tissue perfusion and hypoxia [11]. Mathematical models of oxygen transport in capillaries date back to 1919, with advent of the Krogh cylinder model [12]. Further development of these models to include such phenomena as erythrocyte associated transport (EATs), red cell deformability, and hematocrit, resulted in accurate estimations of tissue oxygen spatial and temporal maps as supported by experimental data [13, 14]. The discovery that oxygen transport is maximized at the arteriolar level lead to the development of very different models to predict the radial and axial gradients responsible for tissue oxygenation [11, 14]. Experimental evidence from phosphorescence quenching and estimations from these mathematical models have lead to a very complete understanding of tissue oxygenation in the microcirculation. Research in oxygen transport in the microcirculation has recently shifted to understanding and developing blood substitutes for transfusion, like HBOCs and polymerized hemoglobin [2].

Applications of the biomechanical and physiological understanding of the microcirculation developed over the past century have been limited to animal models and blood rheology. However, as imaging modalities begin to approach the resolution required to image the microcirculation in patients, the clinical relevance of the microcirculation begins to increase. Currently, techniques to image the microcirculation and obtain quantitative metrics of microvascular perfusion in patients are in clinical trial, further emphasizing the clinical relevance of microcirculation research [15]. The objective of this thesis is to provide insight into the physiology and microvascular hemodynamics of the microcirculation by presenting in vivo data of well-known microcirculatory phenomena.

The first chapter presents a published study on the effects of the endothelial glycocalyx layer (EGL), a complex layer of proteoglycans and glycoproteins, on microvascular hemodynamics via its enzymatic degradation. In this study, we evaluated the hypothesis that as the EGL determines CFL dynamics, blood flow, and shear rates, it consequently affects blood apparent viscosity. By

degrading the EGL, we investigate in vivo the non-Newtonian relationship between shear rate and shear stress of blood flow in microvessels to establish the implications of the EGL on vascular resistance. The data presented in this chapter provide insight into human pathophysiologies that affect the EGL, like diabetes, and suggest alternative therapeutic mechanisms for treatment.

The second chapter presents work investigating the effects of systemic hematocrit on microvascular hemodynamics, particularly the effects of hemoconcentration and hemodilution on blood flow and the arteriolar cell free layer. The results from this study have clinical implications on the changes in hemodynamics and cardiovascular dependent parameters in the context of pathophysiologies associated with changes in hematocrit, namely anemia and polycythemia. An elevated blood viscosity is associated with polycythemia, which is implicated in many disorders, including vascular disease and myocardial infarction. These changes were found to be associated with a decrease in tissue perfusion and were implicated in the tissue damage following injury. Epidemiological evidence indicates that patients with high hematocrit are prone to limited perfusion, vascular occlusive disease, and impaired collateral perfusion and penumbral salvage.

With the advent of deep learning and its implications in image processing, it becomes useful to analyze the data obtained from in vivo microcirculatory studies from high-speed intravital microscopy videos of window chamber models. These types of analyses provide methods for obtaining high spatial and temporal resolution data of microvascular hemodynamic parameters, like velocity and shear rate. However, deep learning implementations of image analysis are severely limited due to the large number of videos required for training. Consequently, the final chapter of this thesis presents improved computer vision and image processing techniques developed to analyze the spatial variations in the arteriolar cell free layer within a single vessel. As such analysis has never been performed on experimental data from the microcirculation, we are hopeful that application of these new techniques may provide further insight into the physiology of oxygen transport as a function of CFL thickness in the microcirculation.

Chapter 1

Implications of Enzymatic Degradation of the Endothelial Glycocalyx on the Microvascular Hemodynamics and the Arteriolar Red Cell Free Layer of the Rat Cremaster Muscle

Abstract: The endothelial glycocalyx is a complex network of glycoproteins, proteoglycans, and glycosaminoglycans; it lines the vascular endothelial cells facing the lumen of blood vessels forming the endothelial glycocalyx layer (EGL). This study aims to investigate the microvascular hemodynamics implications of the EGL by quantifying changes in blood flow hydrodynamics post-enzymatic degradation of the glycocalyx layer. High-speed intravital microscopy videos of small arteries (around 35μm) of the rat cremaster muscle were recorded at various time points after enzymatic degradation of the EGL. The thickness of the cell free layer (CFL), blood flow velocity profiles, and volumetric flow rates were quantified. Hydrodynamic effects of the presence of the EGL were observed in the differences between the thickness of CFL in microvessels with an intact EGL and glass tubes of similar diameters. Maximal changes in the thickness of CFL were observed 40min post-enzymatic degradation of the EGL. Analysis of the frequency distribution of the thickness of CFL allows for estimation of the thickness of the endothelial surface layer (ESL), the plasma layer, and the glycocalyx. Peak flow, maximum velocity, and mean velocity were found to statistically increase by 24, 27, and 25%, respectively, after enzymatic degradation of the glycocalyx. The change in peak-to-peak maximum velocity and mean velocity were found to statistically increase by 39 and 32%, respectively, after 40 min post-enzymatic

degradation of the EGL. The bluntness of blood flow velocity profiles was found to be reduced post-degradation of the EGL, as the exclusion volume occupied by the EGL increased the effective volume impermeable to RBCs in microvessels. This study presents the effects of the EGL on microvascular hemodynamics. Enzymatic degradation of the EGL resulted in a decrease in the thickness of CFL, an increase in blood velocity, blood flow, and decrease of the bluntness of the blood flow velocity profile in small arterioles. In summary, the EGL functions as a molecular sieve to solute transport and as a lubrication layer to protect the endothelium from red blood cell (RBC) motion near the vessel wall, determining wall shear stress.

1.1 Introduction

Blood is a multiphase fluid, consisting of red blood cells (RBCs), plasma, proteins, and electrolyte, with nearly 45% of blood volume occupied by RBCs. Consequently, the resistance to blood flow and blood apparent viscosity are largely dependent on the shear stress experienced by RBCs [16]. Hydrodynamic forces during blood flow force RBC migration away from the vessel wall, generating a RBC depleted zone near the vessel wall, or cell free layer (CFL), and a RBC packed core near the center of the blood vessel [17]. The formation of the CFL in flowing blood is an important hemodynamic feature of blood flow in the microcirculation. The CFL corresponds to a low viscosity zone, which acts as a lubricating hydrodynamic layer, reducing resistance to flow between the central core of RBCs and the vessel wall [16, 18]. The thickness of the CFL is proportional to the yield stress of the flowing fluid and depends on the hematocrit (Hct), RBC aggregation, vessel geometry, the migration forces driving the RBCs to away from the vessel wall, and the endothelial glycocalyx.

The endothelial cells lining the luminal side of blood vessels are covered with membrane-bound macromolecules, glycoproteins, and proteoglycans known as the endothelial glycocalyx. The polyanionic nature of the glycocalyx is a consequence of the glycoproteins, bearing acidic oligoasaccharides and terminal sialic acids (SAs) and the proteoglycans, with their glycosamino-

glycan (GAG) side chains, that compose it. As such, under physiological conditions the glycocalyx is negatively charged. Association of the polyanionic components of the endothelial glycocalyx layer (EGL) with blood-borne molecules results in an extended endothelial surface layer (ESL) that arises from the EGL [19, 20]. Enzymes and their inhibitors, growth factors, plasma proteins, cytokines, cations, and water, all associate with this matrix of biopolyelectrolytes [21, 22]. In addition to glycoproteins, proteoglycans and GAGs, the EGL mainly consists of keratan sulfate, chondroitin sulfate, dermatan sulfate, heparan sulfate, and hyaluronan. The EGL provides selective vasoprotective barrier properties of the vascular wall against vascular leakage, platelet, and leukocyte adhesion [23]. In intact blood vessels, the glycocalyx has an important role in a wide range of physiological processes including increasing vascular permeability, sensing shear stress, and impeding leukocyte and platelet adhesion to the vessel wall [23, 24]. *In vivo* observations have reported a structure named the ESL, which includes the glycocalyx and other plasma proteins attached to the glycocalyx [20]. The ESL thickness has been reported to be approximately range from 0.5μm to over 1μm [24]. In general, reports suggest that the ESL thickness varies in different regions of the vascular network [25]. It is well known that an ESL exists but *in vivo* thickness of the layer is controversial because of the different values from the different techniques in the literature.

This study was conducted to evaluate the effect of the EGL on microvascular blood flow in small arterioles using the rat cremaster muscle preparation. The endothelial glycocalyx was enzymatically degraded by enzymatic degradation via systemic infusion of enzymes to cleave specific GAGs (heparinase, chondroitinase, and hyaluronidase). The degradation of the EGL did not produce major changes in the main systemic parameters of the studied animals. We evaluated the hypothesis that as the EGL determines CFL dynamics, blood flow, and shear rates, it consequently affects blood apparent viscosity. By degrading the EGL, we investigate *in vivo* the non-Newtonian relationship between shear rate and shear stress of blood flow in microvessels to establish the implications of the EGL on vascular resistance. Responses to changes in the integrity

of the EGL were studied for individual arterioles using intravital microscopy and capturing high-speed video recordings to measure the CFL thickness and blood flow velocity. *In vivo* blood flow measurements were combined with CFL thickness assessment with sufficient spatial and temporal resolution.

1.2 Materials and Methods

1.2.1 Animal Model and Tissue Preparation

Sprague-Dawley rats (Harlan Laboratories, Livermore, CA) weighing 150185g were used to perform the studies. Experiments were approved by the Institutional Animal Care and Use Committee at University of California San Diego and conducted in accordance with the Guide for the Care and Use of Laboratory Animals [26]. The cremaster muscle model, for which the complete surgical preparation is elsewhere described in detail, was used for observation of the microcirculation [27]. Briefly, 60 mg/kg pentobarbital sodium was injected ip for anesthesia of rats. Throughout the experiment, additional anesthesia was administered as needed. Blood withdrawals and pressure measurements were obtained from the catheterized femoral artery. Catheterization of the right jugular vein was utilized for fluid and anesthesia administration. The animal was positioned on a stage where the cremaster muscle was gently lifted and secured by sutures on a temperature controlled plexiglass pedestal (Physitemp Instruments, Inc. Clifton, NJ). Plastic film was used to cover the exposed muscle (Saran, Dow Corning, Indianapolis, IN). Arteriole responsiveness to a physiological stimulus was tested by topically applying adenosine (10^4 M) mixed with suffusate under the polyvinyl film. The experimental procedures were started after 2030 min after the adenosine was washed away. Non-reactive vessels or vessels not recovering baseline diameter within this time period were excluded from study. Similarly, at the end of the study, adenosine (10^4 M) was reapplied and non-reactive vessels, or vessels that had not recovered their diameter prior adenosine application 20 min after washing it, were excluded

from study. At the end of the experiment, animals were euthanized.

1.2.2 Intravital Microscopy

The experimental setup consisted of an intravital microscope (Olympus-BX51WI) equipped with a matching long working distance condenser (NA = 0.8, Thorlabs, Newton, NJ). Two magnifications of 2X and 1.5X were installed between the objective (40X, LUMPFL-WIR, NA = 0.8; Olympus) and the high-speed camera, providing a total magnification of 1200X with an equivalent resulting pixel size of 0.125 m relative to the object plane. A mercury arc lamp (100 W, Walker Instruments, Scottsdale, AZ) was used to illuminate the tissue. A 400- nm interference filter (Spectra Physics, no. 59820) was placed above the condenser in the light path to maximize contrast between blood and the surrounding tissue. A high-speed video camera (Fastcam 1024 PCI, Photron USA), equipped with a one- megapixel chip was used for video recording. Additionally, all videos were recorded between 2,000 and 3,000 frames per second and the camera shutter speed was optimized to obtain the highest quality image possible.

1.2.3 Experimental Protocol

As blood rheology is strongly influenced by hematocrit (Hct), the systemic Hct of all animals included in the study was standardized to 40% Hct via hemodilution when needed. Hemodilution was accomplished by concurrent withdrawal of blood from the arterial catheter and infusion of 5% wt/v human serum albumin solution (ABO Pharmaceuticals, San Diego, CA) using the venous catheter. Vessel diameter was continuously monitored, and video recordings for velocity measurements were collected at selected time points.

1.2.4 Microvascular Diameter and Cell Free Layer (CFL) Thickness

The analysis of intensity along a video raster line across the vessel was used to determine the vessel diameter (D), RBC column width, and CFL thickness. Detailed information of the

algorithm has been previously described [28]. he CFL thickness was approximated as the distance between the outer edge of the RBC core and the vessel wall. CFL analysis was performed on both sides of the vessel using a sequence of 1,600 consecutive video frames. Diameter and CFL were measured over a 0.8 s time. Vessel diameter was averaged over this period, and only diameters with standard deviation close to zero were used. Diameter measurements with high standard deviation were discarded and repeated, as diameters were not expected to change over this short period. CFL temporal variation (TV) was defined as the standard deviation of the CFL measurements in an entire image sequence divided by the time elapsed [29].

1.2.5 Blood Velocity Profiles

The instantaneous blood flow velocities at different points along the radial direction of the micro-vessel were determined from velocity profiles measured using 2D cross correlation. Briefly, images are segmented (10×10 pixels), and the displacement of each segment relative to the subsequent image is calculated based on the maximum correlation coefficient, from which cross correlation coefficients are calculated. Velocity was calculated as the longitudinal displacement multiplied by the frame rate (2,000 fps). This approach provides a spatial velocity profile for every set of two consecutive frames and allows for a range of velocity measurements between 0.3 and 250 mm/s. Mean velocity was calculated as the arithmetic mean of the velocity profile. Blood flow (Q) was calculated assuming Poiseuilles flow, as:

$$Q = \frac{\pi D^4 V}{4} \tag{1.1}$$

where D is the vessel diameter, and V is the mean blood flow velocity.

1.2.6 Enzymatic Degradation of the Endothelial Glycocalyx

Enzymatic degradation of the glycocalyx in the cremaster muscle is achieved by systemic infusion of specific enzyme cocktail. Specific GAGs were cleaved by the enzymes heparinase III

(50 U/mL), chondroitinase ABC (10 U/mL) and hyaluronidase (3,000 U/mL) and were given in bolus doses via the femoral catheter [30]. CFL recordings were made at 5, 20, 40, and 60min after enzyme treatment and for a sham group at the same timepoints. This treatment was selected as it is reported not to produce any significant changes in the main systemic parameters of the studied animals.

1.2.7 Estimation of the Endothelial Glycocalyx Thickness

EGL thickness was estimated by subtracting the 99% confidence interval of the CFL in a glass tube, in which only fluid hydrodynamic forces from the 99% confidence interval measured *in vivo*. As the CFL is the sum of the effects of the EGL and the fluid hydrodynamic forces, subtraction of the two distributions will yield an approximation of the thickness of the endothelial glycocalyx. However, because the glycocalyx itself has hydrodynamic forces associated with its presence, it is impossible to exactly determine the thickness of the glycocalyx utilizing this methodology.

1.2.8 Velocity Profiles

Velocity profiles were determined via auto-correlation of high- speed intravital microscopy videos before and after enzymatic degradation of the endothelial glycocalyx, and results were fit to the following model:

$$v(r) = v_{\max}\left(1 - \left|\frac{r}{R}\right|\right)^{K} \tag{1.2}$$

where $v(r)$ is the spatial velocity profile, vmax is the maximum velocity of the profile,R is the radius of the vessel, and K is the blunting coefficient. Least squared fits were determined using the MATLAB Curve Fitting Toolbox [31].

1.2.9 Statistical Analysis

Results are presented as mean standard deviation. All statistical calculations and graphics were performed with a commercially available software package (Prism 7.0, GraphPad). To test the normality of the distributions, the DAgostino and Pearson Normality test was used. Groups comparisons were performed for diameter and CFL thickness data utilizing both ordinary one-way ANOVA. In this case, the assumption of normality in the ANOVA test-statistic was validated via the non-parameterized Geisser Greenhouse test to test for sphericity. As the sphericity metric for all comparisons approached 1, it can be concluded that the ANOVA test statistic is Gaussian, even though the original distributions for CFL thickness were non-Gaussian. Pair-wise comparisons for velocity and flow data were performed with a Mann-Whitney U -Test. Variance comparisons were performed utilizing the F-test. For all tests, $P < 0.05$ was accepted as statistically significant. Histograms and cumulative distribution functions (CDFs) of the CFL were numerically determined and analyzed at different time points. The maximum likelihood of the CFL thickness was approximated as the inflection point of the CDF. Ninety nine confidence intervals are presented from the point at which $P = 0.01$ to the maximum likelihood determined from the CDF. A Bland Altman analysis was utilized to analyze variations in CFL thickness over time as compared to a glass tube:

$$S(x,y) = \left(\frac{S_1 + S_2}{2}, S_1 - S_2\right) \tag{1.3}$$

Where S_1 is the thickness of the CFL at baseline and after enzymatic degradation, and S_2 is the thickness of the CFL in a glass tube. All animals passed the Grubbs test, ensuring that all the measured values at baseline were within a similar population ($P < 0.05$).

1.3 Results

A total of 27 animals (n = 27) were entered into the study, two or three arteries were selected in each animal. After application of the systemic and vessel reactivity inclusion criteria, data from 20 animals (n = 20) were in included in the results. We found no significant differences in the systemic parameters, confirming that the EGL degradation only had microvascular effects without causing systemic hemodynamic disturbance. Additionally, **Table 1.1** presents the thickness of the CFL after enzymatic treatment and in a Control group over time. As demonstrated in the sham group variations in the CFL thickness were within $\pm 5\%$ of that at baseline, while the CFL thickness decreased by 11.4% 40min after enzymatic treatment. These results provide sufficient evidence that changes in the thickness of the CFL were likely due to enzymatic treatment and not due to spontaneous variations.

Table 1.1: Thickness of the CFL after enzymatic treatment and control groups.

	Baseline	**5 min**	**20 min**	**40 min**	**60 min**
Control (% change from BL)	$2.04 \pm 0.01\,\mu$m (0.0%)	$2.13 \pm 0.01\,\mu$m (+4.6%)	$2.11 \pm 0.01\,\mu$m (+3.4%)	$2.06 \pm 0.02\,\mu$m (+0.8%)	$1.98 \pm 0.01\,\mu$m (-3.1%)
Enzyme Treatment (% change from BL)	$2.76 \pm 0.02\,\mu$m (0.0%)	$2.93 \pm 0.02\,\mu$m (+7.8%)	$2.50 \pm 0.01\,\mu$m (+-5.8%)	$2.42 \pm 0.02\,\mu$m (-11.4%)	$3.22 \pm 0.02\,\mu$m (+18.4%)

1.3.1 CFL Analysis for a Single Blood Vessel

Initial arteriole diameter was 3436 μm and maximally decreased to 3233 μm 20 min after enzymatic degradation of the glycocalyx. No change in diameter was detected in the Control group overtime relative to baseline. The maximal change in diameter measured was $< 5\%$ from baseline diameter at 20 min after enzymatic degradation of the glycocalyx. The reduction in diameter increases the fraction of the radius of the arterioles occupied by the CFL from 5.8 to 6.1%. Image analysis of high- speed intravital microscopy videos recorded for a single arteriole was quantified in terms of the CFL thickness at different time points after infusion of the enzyme

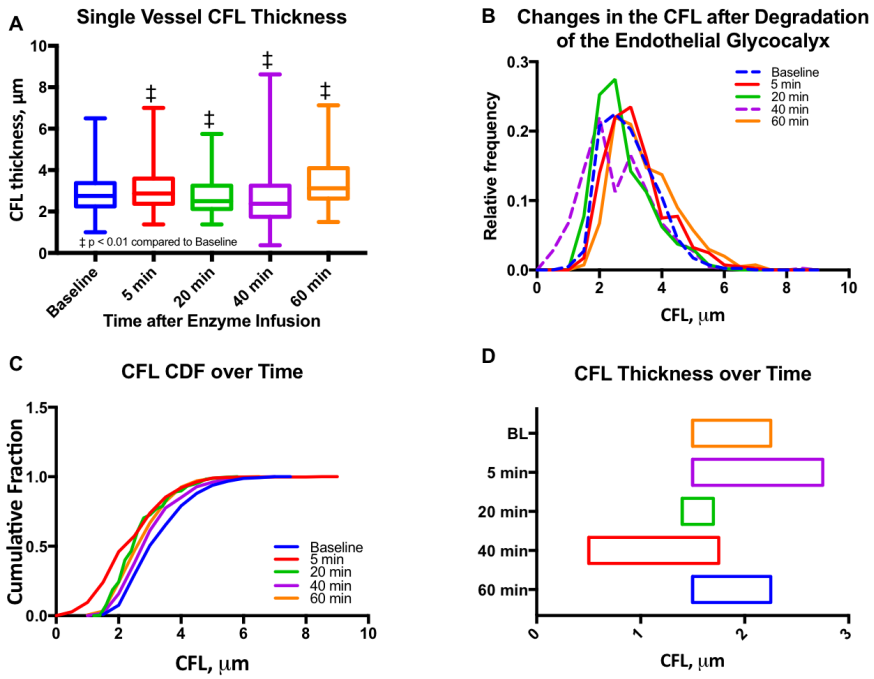

Figure 1.1: Single microvessel CFL thickness during enzymatic degradation of the EGL: **(A)** CFL thickness over time after enzyme infusion. The changes in the mean CFL were found to be statistically significant ($^{\ddagger}P < 0.05$) at all-time points. **(B)** Histograms of CFL thickness over time after enzyme infusion. **(C)** Cumulative distribution functions (CDF) of CFL thickness over time after enzyme infusion. **(D)** One tailed 99% confidence interval of CFL over time after infusion. The left hand bound was determined as the point on the CDF at which $P < 0.01$, and the right hand bound was determined as the inflection point of the CDF (see **Supplemental Figure 1.8**). ($^{\ddagger}P < 0.05$) compared to baseline.

cocktail (**Figure 1.1**). Thickness of the CFL is presented in **Figure 1.1A**. The CFL thickness was found to be statistically different from baseline at all-time points. The median value of the CFL thickness decreased to 86% of that at baseline at 40min after enzymatic degradation of the glycocalyx. Distributions of the CFL thickness were also found to deviate from a standard Gaussian to a right-skewed distribution, indicative of the vessel wall acting as a physical boundary to blood flow as the distributions failed the Kolmogorov-Smirnov and the DAgostino and Pearson Normality Test, $P < 0.001$ (**Figures 1.1 B,C**). Differences in the variances of the distributions were also found to be statistically significant. The 99% confidence interval of the CFL thickness is presented in (**Figure 1.1D**).

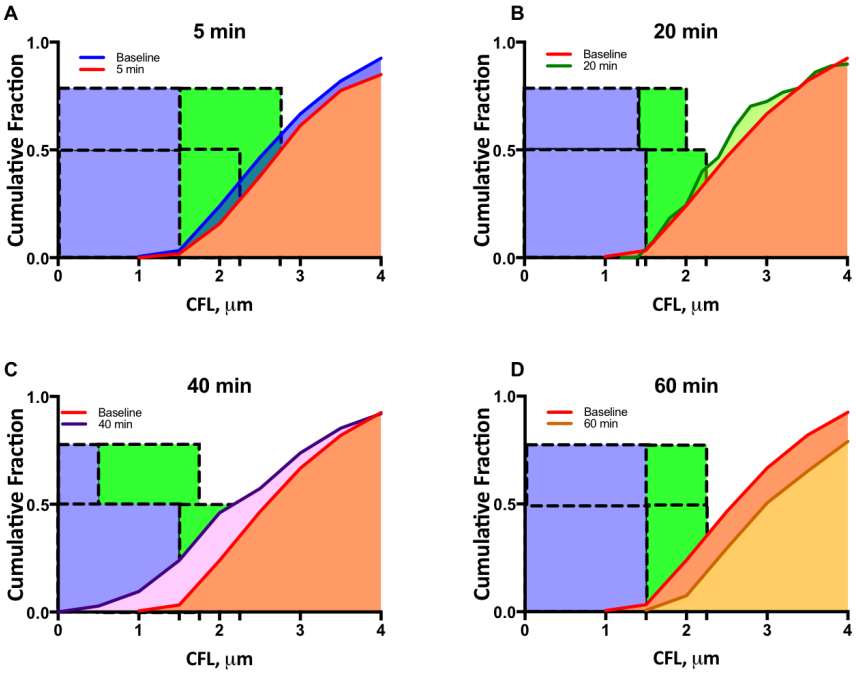

Figure 1.2: Single microvessel cumulative distribution function during enzymatic degradation of the EGL: CDFs at baseline and at **(A)** 5 min, **(B)** 20 min, **(C)** 40 min, and **(D)** 60 min after enzyme infusion. The blue bonding box represents the portion of the CFL influenced by the glycocalyx and its associated hydrodynamic forces, and the green bounding box represents the one-tailed 99% confidence interval of the CFL thickness (see **Supplemental Figure 1.9**).

The cumulative fractions of the CFL over time compared to baseline are presented in **Figure 1.2**. The 99% confidence interval of the CFL was found to decrease from $\delta \in [1.50\mu\text{m}, 2.25\mu\text{m}]$ to a low of $\delta \in [0.50\mu\text{m}, 1.75\mu\text{m}]$ at a time of 40 min, where is the thickness of the CFL. Additionally, thickness of the CFL increased between 40 and 60 min to $\delta \in [1.50\mu\text{m}, 2.25\mu\text{m}]$, indicating recovery of the endothelial glycocalyx.

1.3.2 CFL Analysis From Multiple Blood Vessels

Changes in vascular tone for all the 46 arterioles (ranging from 30 to 36μm) from 20 different animals were not statistically significant at the different time points compared to baseline. The thickness of the CFL for the 46 arterioles is presented in **Figure 1.3A**. Similar to the analysis of a single vessel, there were statistically differences in the CFL thickness over all time points

compared to baseline. The CFL thickness does not fit a Gaussian (normal) distribution, indicating random variation, as the distributions failed the DAgostino and Pearson Normality Test, $P < 0.001$. The distribution of the CFL thickness was observed to be right-skewed, which is due to the vessel wall acting as a physical barrier to the thickness of the CFL (**Figures 1.3 B,C**). The 99% confidence interval of the CFL thickness for 46 arterioles is presented in **Figure 1.3D**. The cumulative fractions of the CFL over time compared to baseline are showed in **Figure 1.4**. The 99% confidence interval of the CFL was found to decrease from $\delta \in [1.00\ \mu\text{m}, 2.25\mu\text{m}]$ to a low of $\delta \in [0.50\mu\text{m}, 1.75\mu\text{m}]$ at a time of 40 min. Additionally, thickness of the CFL increased between 40 and 60 min to of $\delta \in [1.00\mu\text{m}, 2.75\mu\text{m}]$. For reference, the thickness of the CFL in a glass tube was measured and the 99% confidence interval was found to be $\delta \in [0.50\mu\text{m}, 1.75\mu\text{m}]$. In addition, the size of the 99% confidence interval of the CFL was found the statistically larger than that at baseline via the F-test, indicating unequal spatial recovery of the EGL after enzymatic degradation.

1.3.3 EGL Thickness

Glycocalyx thickness was found to be approximately $0.50 \pm 0.02\ \mu$m and was found to degrade to $0.25 \pm 0.02\ \mu$m 20 min after infusion of the enzyme cocktail (**Figures 1.3A, 1.4**).

1.3.4 Variances in CFL Thickness Over Time

Variations in the CFL thickness over time before and after enzymatic degradation of the CFL are shown in **Figure 1.5A** and compared to those in a glass tube of equal diameter in **Figure 1.5B** via a Bland-Altman plot. The mean deviation of the CFL from that of a glass tube statistically decreased after enzymatic degradation of the EGL. The size of the 95% confidence interval did not change after degradation of the EGL. The negative end of the 95% confidence interval changed, while the positive end remained constant, determined by the presence of the vessel wall.

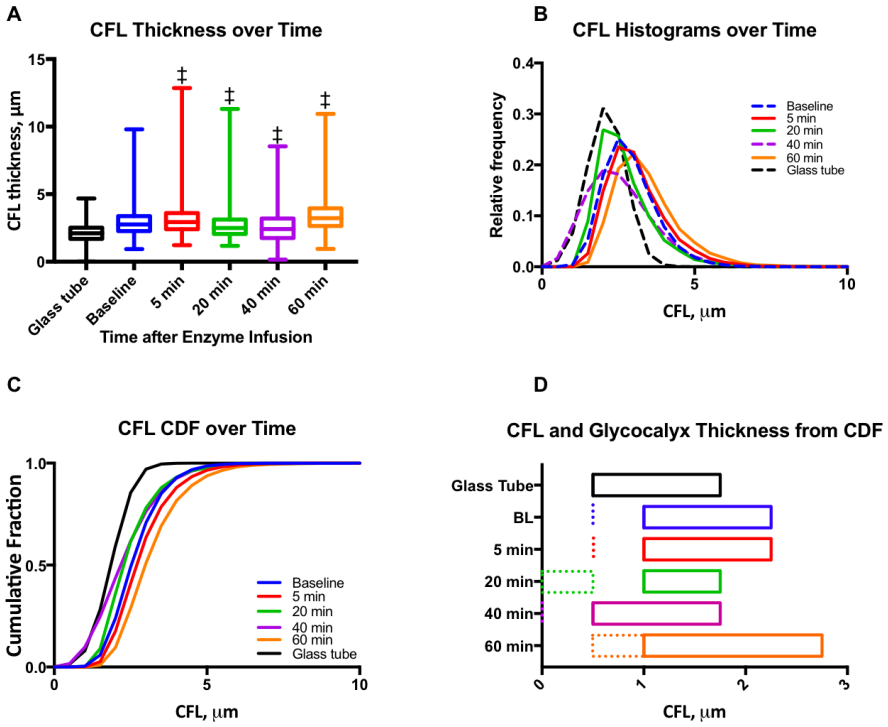

Figure 1.3: Mean CFL thickness during enzymatic degradation of the EGL: **(A)** CFL thickness over time after enzyme infusion. The changes in the mean CFL were found to be statistically significant ($^{\ddagger}P < 0.05$) at all-time points. **(B)** Histograms of CFL thickness over time after enzyme infusion. For individual histograms, see **Supplemental Figure 1.9**. **(C)** Cumulative distribution functions (CDF) of CFL thickness over time after enzyme infusion. **(D)** One tailed 99% confidence interval of CFL over time after infusion. The left hand bound was determined as the point on the CDF at which $P < 0.01$, and the right hand bound was determined as the inflection point of the CDF (see **Supplemental Figure 1.8**). The thickness of the EGL (indicated as dotted line) was approximated by correcting the CFL distributions with that measured for a glass tube, in which only fluid hydrodynamic forces are present. ($^{\ddagger}P < 0.05$) compared to baseline.

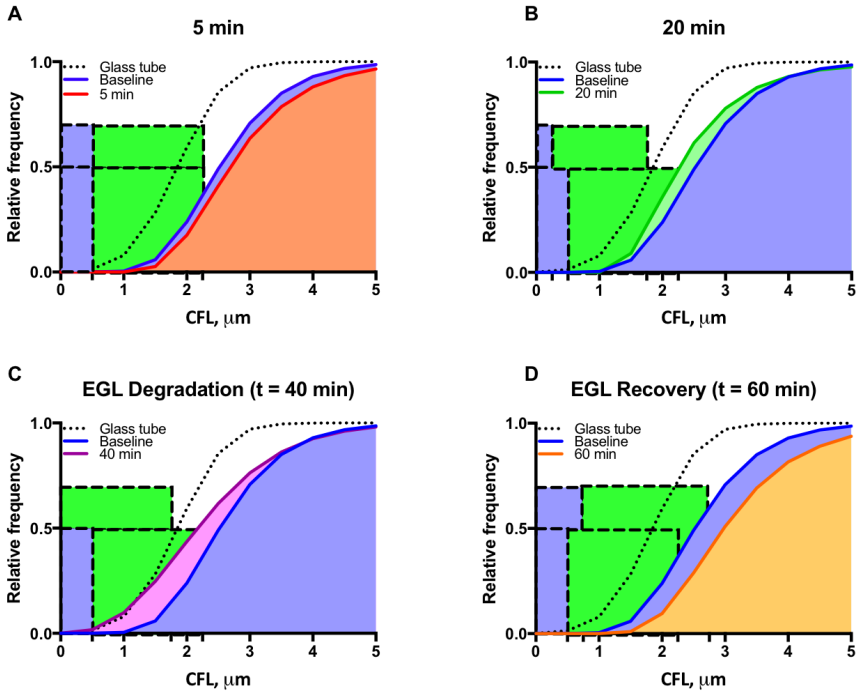

Figure 1.4: Mean cumulative distribution function during enzymatic degradation of the EGL: CDFs at baseline and at **(A)** 5 min, **(B)** 20 min, **(C)** 40 min, and **(D)** 60 min after enzyme infusion. The blue bonding box represents the approximated thickness of the glycocalyx, and the green bounding box represents the one-tailed 99% confidence interval of the CFL thickness.

Comparing the variance of the CFL thickness from the blood vessel to the glass tube before and after enzymatic degradation of the glycocalyx, shows that degradation of glycocalyx increases the difference in the CFL between the blood vessel and the glass tube. The positive end of the difference remained unaltered, because it is indicative of the vessel wall, whereas the negative boundary of the difference shows the increased erratic variations in the CFL of the blood vessel after the degradation of the glycocalyx.

1.3.5 Blood Flow and Blood Velocity Over Time

Max blood flow, max blood velocity, and mean velocity were found to statistically increase by 24, 27, and 25%, respectively, after enzymatic degradation of the EGL. Additionally, the change in peak-to-peak max velocity and peak-to-peak mean velocity between were found to statistically

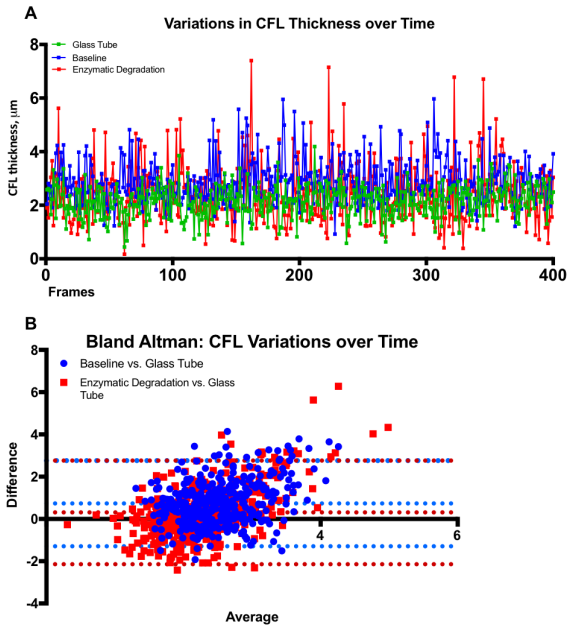

Figure 1.5: Thickness of the CFL over time after enzymatic degradation of the EGL. **(A)** Fluctuations in the thickness of the CFL over time in a glass tube, at baseline, and after enzymatic degradation of the glycocalyx. **(B)** Bland Altman plots comparing the difference of the CFL thickness vs. a glass tube at baseline and after enzymatic degradation of the glycocalyx. The 95% confidence interval of the difference between the CFL of the blood vessels are illustrated with lines. The solid line indicates the positive end of the difference between the CFL of the blood vessels and the glass tube, which remained unaltered as it is determined by the vessel wall. The dotted line indicates the negative boundary of the difference between the CFL of the blood vessels and the glass tube, illustrates the increased erratic variations in the CFL of the blood vessel after the glycocalyx degradation.

increase by 39 and 32%, respectively, after enzymatic degradation of the EGL. However, the increase in the change in peak-to-peak flow was not found to be statistically significant after degradation of the EGL. Results are summarized in **Figures 1.6, 1.7 A,B**.

1.3.6 Velocity Profiles After Enzymatic Degradation of the EGL

Velocity profiles before and after degradation of the EGL are presented in **Figures 1.7 C,D**. During systole, the blunting coefficient decreased from 4.1 ± 0.4 to 3.5 ± 0.7 after enzymatic degradation of the EGL. Similarly, during diastole, the blunting coefficient decreased from 3.1 ± 0.6 to 2.2 ± 0.6 after enzymatic degradation of the EGL. Thus degradation of the EGL

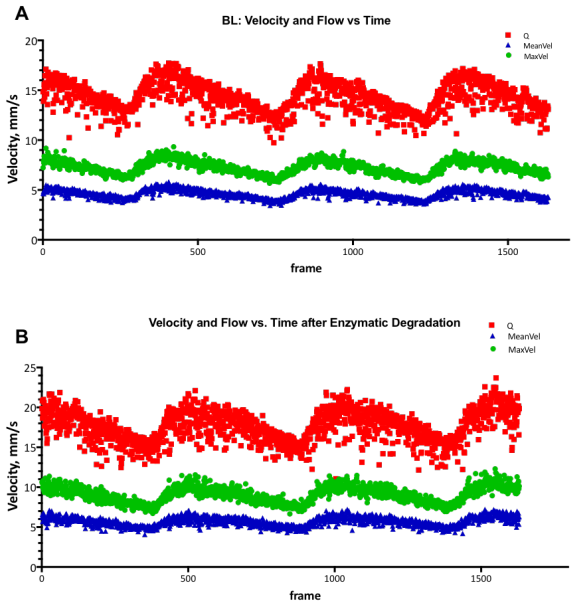

Figure 1.6: Flow, mean velocity, and peak velocity after degradation of the EGL. Flow (Q), mean velocity (V_{mean}), and peak mean velocity (V_{max}) at **(A)** Baseline, and **(B)** after enzymatic degradation of the glycocalyx.

decreased microvessel blood velocity bluntness and a shift toward Poiseuille flow.

1.4 Discussion

The principle finding of this study is that enzymatic degradation of the EGL resulted in a statistically decrease in the CFL thickness, as well as a statistical increase in max blood flow, and max and mean blood velocity. Enzymatic degradation of the EGL also decreased the blunting of the blood velocity profile in arterioles, indicating a shift toward Poiseuille flow. Previous studies have posed models to explain the hydrodynamic and physical forces associated with the EGL [32, 33, 34, 24, 35]. Our study provides *in vivo* validation of the hydrodynamic effects of the EGL on blood flow. Changes in the thickness of the CFL during enzymatic degradation compared to the CFL thickness in glass tubes confirms the physical presence of the glycocalyx and the hydrodynamic lubricating layer it produces, and allows for estimation of the apparent thickness (0.5μm). Literature and mathematical models describe the effects of enzymatic degradation of the

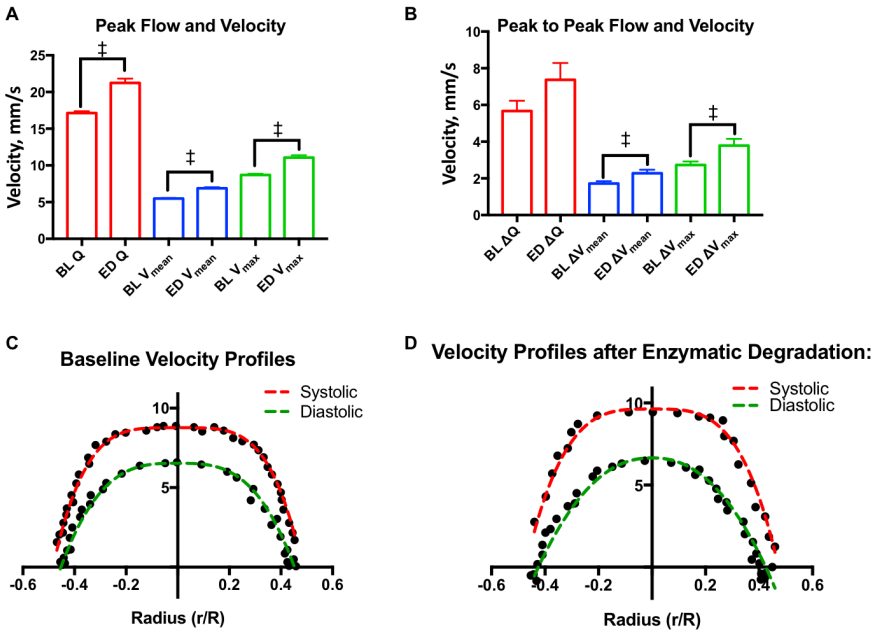

Figure 1.7: Velocity profiles after degradation of the EGL: **(A)** Systolic flow, mean velocity, and peak velocity after degradation of the glycocalyx ($^{\ddagger}P<0.05$). **(B)** Changes in flow (Q), mean velocity (V_{mean}), and peak mean velocity (V_{max}) between systole and diastole after degradation of the glycocalyx ($^{\ddagger}P<0.05$). **(C)** Baseline velocity profiles during systole and diastole. Results were fit to the model $v(r) = V_{\text{max}}(1-|\frac{r}{R}|)^K$. During systole, $V_{\text{max}} = 8.8 \pm 0.2$, $R = 0.48 \pm 0.01$, and $K = 4.1 \pm 0.4$. During diastole, $V_{\text{max}} = 6.5 \pm 0.4$, $R = 0.45 \pm 0.01$, and $K = 3.1 \pm 0.6$. **(D)** Celocity profiles during systole and diastole after enzymatic degradation of the glycocalyx. Results were fit to the model $v(r) = V_{\text{max}}(1-|\frac{r}{R}|)^K$. During systole, $V_{\text{max}} = 9.6 \pm 0.5$, $R = 0.78 \pm 0.01$, and $K = 3.4 \pm 0.7$. During diastole, $V_{\text{max}} = 6.7 \pm 0.7$, $R = 0.43 \pm 0.01$, and $K = 2.2 \pm 0.6$. ($^{\ddagger}P<0.05$) compared to baseline.

EGL on microvascular blood flow as the balance between two opposing forces. As the glycocalyx is a physical barrier to blood flow, it decreases the effective diameter, or the diameter accessible to blood flow, of the lumen. In this schema, degradation of the EGL increases the effective diameter of the lumen, thus decreasing vascular resistance and consequently decreasing blood flow. However, the anionic character of the glycocalyx imparted to it by the glycoproteins and glycosaminoglycans that constitute it are a source of electrical forces that effectively increase the apparent viscosity of blood by forcing negatively charged RBCs toward the center of the lumen, known as the electro- viscous effect. In this schema, degradation of the EGL will decrease the apparent viscosity of blood, increasing blood flow. The effects of the EGL on microvascular

blood flow are a summation of both phenomena. As observed in this study, in the case of a 34μm, blood flow was found to increase with enzymatic degradation of the EGL, indicating that electro-viscous effects are more dominant for arterioles of this size. The thickness of the EGL and ESL are a small fraction of the arteriole lumen diameter, which increases as the arteriole diameter decreases. Therefore, degradation or damages in the EGL have different effects on microvascular blood flow depending on the arteriole diameter, as the electro-viscous effect of the EGL on blood flow becomes less significant in smaller arterioles. The small changes in diameter induced by the enzymatic degradation of the EGL are not responsible for the changes in the CFL thickness or the hemodynamics measured in the study; although, the vasoconstriction induced by the degradation of the EGL is a confounding effect that overestimates the fraction of the arteriole lumen occupied EGL.

The analyzed video recordings determined arteriolar blood flow using spatial cross-correlation analysis, which allows for measurements of blood flow velocities up to 40 mm/s with a precision that ranges between 0.5 and 1 μm [36]. Arteriolar diameters exhibited minimal variations during the experiments after enzyme treatment. As such, arteriolar blood flow velocity was used to estimate relative changes in network flow resistance. Enzymatic degradation of the EGL decreases the plug flow behavior of the blood velocity profile shifting toward pipe flow behavior, as demonstrated by the decreasing magnitude of the blunting coefficient (**Figures 1.7 C,D**). These results are once again in accordance with the electro-viscous effects produced by the EGL as the electrical forces present in the CFL invalidate the no-slip boundary condition that defines pipe flow. As degradation of the EGL decreases the magnitude of the electrical forces present in the CFL, pipe flow is observed after degradation of the glycocalyx, as the no-slip boundary condition is now valid. This paradigm can also be explained with respect to a classical fluid dynamics model posed by Damiano et al. in which the presence of the EGL promotes Darcy flow in the CFL by increasing the velocity gradients in the plasma interface, thus increasing viscous drag forces in the CFL [37, 38]. In addition to providing a mechanism for the mechanotransductive

behavior, the presence of Darcy flow in the CFL invalidates the no-slip condition, necessary for pipe flow [37, 39]. The EGL is thought to behave as a porous material with a high hydraulic resistance, and consequently plasma velocity through the EGL is very limited; although RBCs essentially slide over the EGL. Thus, degradation of the EGL could increase vascular resistance via preventing RBCs from gliding over the vessel wall.

Enzymatic degradation of the glycocalyx directly affects the ESL, the active composite of bound plasma constituents attached to the EGL. The ESL *per se* influences blood cell- vessel wall interactions, affects blood rheology, and determines solute transport out of the vessel lumen. The ESL function has been suggested to safeguard the fragile EGL from fluid shear stress and from direct physical interactions with blood cells [40]. Increased endothelial shear increases nitric oxide (NO) production, dilating vessels and reducing shear stress [41]. Additionally, it has been observed that under shear stress, human umbilical vein endothelial cells double the hyaluronic acid in the endothelial glycocalyx, suggesting a secondary mechanism by which the vascular endothelium responds to shear stress [42]. As the EGL is exposed to the shear stress of the plasma layer, a function of both the shear rate at the surface of the glycocalyx and the plasma viscosity, the surface of the ESL is exposed to the shear stress of the adjacent whole blood. The resultant effect on the signal transduction pathways of the endothelium could then be combined effects of fluid shear stress on both layers. Previous studies on relationship between the ESL in capillaries and flowing blood demonstrate that the ESL can be highly deformable [34]. However, the finite resistance to compression of the ESL prevents direct plasma shear stress to be generated by blood flow on endothelial cells by decreasing plasma fluid movement within the ESL [20]. The plasma shear stress cannot be transmitted to the ESL as a fluid shear stress; rather, the ESL transfers its shear strain to the structures forming the ESL [40]. Enzymatically degrading the EGL impairs transduction of plasma fluid shear stress and solid shear stress in the ESL, which are both potential mechanisms of endothelial shear stress mechanotransduction [43]. Therefore, endothelial cell surface shear stress transmitted to through the ESL, or plasma fluid shear stress

within the ESL, remain plausible as the mechanism of blood flow mediated mechanotransduction by endothelial cells.

In addition, in capillaries, the ESL creates a large repulsive forces that supports the movement of RBCs by acting as a lubrication layer, which reduces capillary blood flow resistance [35, 44]. This observation highlights the role of the EGL in microvascular perfusion. Pathophysiological degradation of the EGL would increase capillary blood flow resistance by decreasing the thickness of the lubrication layer provided by the EGL. Recent studies have demonstrated that in chronically obese subjects, diabetic subjects, and subjects with coronary microvascular disease, the EGL is found to be thinner as compared to healthy subjects, resulting in impaired vasomotor activity, increased vascular permeability, and decreased perfusion. Additional studies have demonstrated marked improvement in perfusion in animal models with coronary microvascular disease by increasing recovery of the glycocalyx with metformin and sulodexide [45]. Therefore, as the ESL and the glycocalyx decrease capillary blood flow resistance, it seems plausible that pathophysiological degradation of the EGL may play a role in decreased perfusion associated with obesity and related pathophysiologies and influence further progression of these pathophysiologies [45].

Various approaches have been used directly to visualize or estimate the EGL due to the increased recognition of its functional importance. Groups have labeled the glycocalyx with specific markers that attach to one or more of its components, making them fluorescent or detectable [46]. This demonstrates the presence of the EGE, or its components, but it does not establish the thickness of the EGL. Unfortunately, the EGL is easily disturbed and very vulnerable to dehydration. Consequently, the EGL dimension is easily underestimated; early studies estimated EGL thickness to be approximated 20 nm in capillaries using transmission electron microscopy (TEM) [47]. Other attempts using TEM reported the EGL to be around 40 nm [48]. These early estimations did not conform to experimental and theoretical estimation however, suggesting that the EGL should be nearer 1 μm [46, 49]. The thickness of the EGL remains controversial, as resent studies with fluorescent labeling and high-resolution fluorescent

micro-particle image velocimetry suggest that the GGL is around 0.5μm in post-capillary venules of the rat mesenteric and the mouse cremaster muscle, both using intravital microscopy [50, 51]. Recently, new imaging protocols using fluorescently tagged antibodies to heparan sulfate and hyaluronan has revealed a much thicker EGL, over 4.0μm in the mouse common carotid artery [52], 2.2μm in the internal common carotid artery [53], and 2.5μm in the external carotid artery [54]. Most recently, cryo-TEM, which avoids the dehydration artifacts of early TEM, has suggested that the thickness of the EGL is of the order of 10m on cultured endothelial cells in vitro [55]. Therefore, the thickness of the EGL measured from our method is in good agreement with both the classical method for measurement of the EGL and other indirect methods [24]. The approach used in this manuscript to estimate the EGL based on the hydrodynamic implications that the presence of the EGL has in the thickness of the CLF relative to glass tubes of similar diameters. The estimation of the EGL presented in here could differ from the physical thickness of the EGL; although it corresponds to the functional hydrodynamic layer that affect blood flow and exchanges between the flowing blood and the tissues.

The EGL affects blood apparent viscosity in microvessel via the CFL thickness, which is the region with much lower viscosity than the lumen core heavily populated with pack RBCs. Variations in the thickness of the CFL are a consequence of both the Fahraeus effect and the FahraeusLindqvist effect [7]. In the microvasculature ($< 40\mu$m), the CFL thickness is significant percentage of the microvessel tube diameter, resulting in smaller microvessels having a lower relative apparent viscosity compared to larger vessels ($> 40\mu$m). The effects of the EGL with respect to the Fahraeus effect have an impact on oxygen flux to tissues and NO scavenging by hemoglobin in the RBCs, as the EGL contributes to the separation of RBCs from the vascular endothelium. The separation of blood flow between the vessel lumen core, rich of RBCs, and the endothelium, by the CFL zones affects oxygen delivery and NO consumption by RBCs. Computational models for oxygen and NO transport indicate that the CFL determines resistance to diffusion of oxygen and NO to and from RBCs [56, 57]. In addition, the CFL thickness

becomes more important for controlling and enhancing oxygen release and NO bioavailability to both the surrounding tissue and the vascular wall in microvessels with diameters of 30μm or less [56]. The glycocalyx might have additional effects in NO transport, as it modulates vessel wall shear stress-dependent NO production by the endothelium.

The blood flow velocity profiles appear to be a function of the CFL thickness, and therefore in the vessel wall shear stress on the endothelium walls. The thickness of the CFL and its variability is demonstrated by fluctuations in pressure about the mean, as quantified by the standard deviation of the pressure wave. Consequently, changes in CFL thickness counteract changes in blood flow; as CFL thickness increases, volumetric blood flow rate decreases. Volumetric blood flow rate also decreases as the correlation length decreases and/or the standard deviation of the amplitude increases. The mean shear rate can also increase with fluctuations in the endothelium and the CFL. Increasing or decreasing fluctuations in the endothelium can also extend the entrance length (the length through which the flow regime is not fully-developed, and shear stress statistics are constant). Thus, blood viscosity, estimated from *in vivo* experiments by Poiseuilles law, depends not only on the rheological properties of blood, but also by the statistical parameters that quantify endothelium roughness.

The distribution of plasma and RBCs at the vascular wall has traditionally been attributed to the Fahraeus effect and axial migration of red cells [7]. However, it is now well established that ESL also importantly affect this distribution [20]. The ESL significantly restricts the approach of RBCs and plasma to the vascular wall [29]. This study was conducted to evaluate the effects of the effects of enzymatic degradation of the EGL on blood flow via preparation of the rat cremaster muscle. We evaluated the hypothesis that enzymatic degradation of the EGL resulted in variations and reductions of the CFL, increased randomness of blood flow, and variations in the observed microhemodynamics. By measuring the change in the thickness of the CFL over time after degradation as well as the probability distribution of RBCs as a function of distance, it is possible to establish a relationship between the micro hemodynamic properties of blood flow

and the EGL. Recent studies have demonstrated that the glycocalyx influences homogenous flow distribution in the microcirculation [58]. In addition, many recent studies have implicated the alterations in the mechanotransductive effects of the EGL under different pathophysiological conditions, including inflammation, diabetes, and atherosclerosis [59]. As such, future studies should investigate changes in the hemodynamics under these pathophysiological conditions that result due to alterations in the EGL utilizing *in vivo* models.

1.5 Conclusion

These results demonstrate that enzymatic degradation of the EGL results in a statistically significant increase in flow and mean velocity as well as a decrease in the bluntness of the velocity profile in the microcirculation. In addition to providing in vivo validation of many mathematical models that explain the hydrodynamic effects of the EGL, these results suggest that the EGL is responsible for alterations in blood flow in microvessels via both the electrical and hydrodynamic fluid forces that it produces. Future studies should investigate the changes in hydrodynamics associated with pathophysiological alterations in the EGL.

1.6 Supplemental Information

The Supplementary Material for this article can be found below:

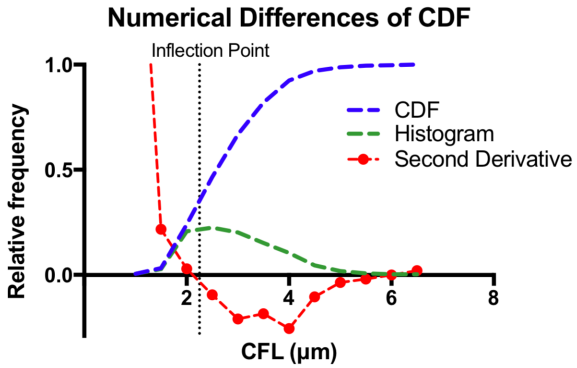

Figure 1.8: Numerical differences of the cumulative distribution function of the CFL thickness. To determine the inflection point of the CDF, the second numerical difference of order 4 was determined, and the bisection method was used to determine the root of the second derivative.

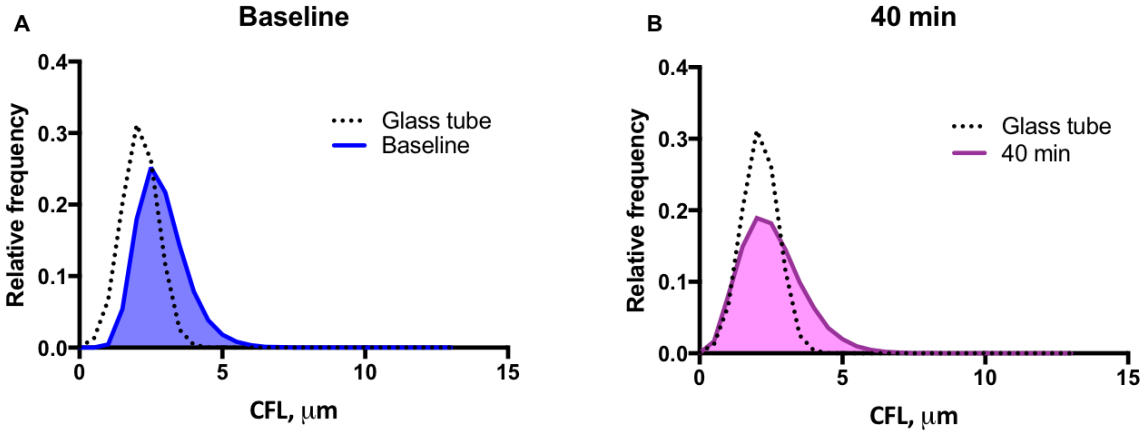

Figure 1.9: Mean histograms of the thickness of the CDF. Histograms of the thickness of the CDF during **(A)** Baseline, and **(B)** 40 min after enzyme infusion.

Chapter 1, in full, is a reprint of the material as it appears in Implications Enzymatic Degradation of the Endothelial Glycocalyx on the Microvascular Hemodynamics and the Arteriolar Red Cell Free Layer of the Rat Cremaster Muscle 2018. Yalcin, O., Jani, V. P., Johnson, P. C., & Cabrales, P. Frontiers in Physiology, 9, 168. http://doi.org/10.3389/fphys.2018.00168. The thesis author was the primary investigator and author of this paper.

Chapter 2

Implications of Systemic Hematocrit on Microvascular Hemodynamics, From Blood Flow to the Radial Distribution of Red Cells and Plasma in Microvessels

Abstract: This study focuses on the effects of hemoconcentration and hemodilution on blood flow in small arterioles, which are the mayor contributors to vascualar resistance. Hemoconcentration was induced by exchange transfusion with fresh RBCs in increments of 5% hematocrit (Hct), while hemodilution was induced by exchange transfusion with fresh plasma in decrements of 5% Hct. Utilizing high resolution, high speed video microscopy, and computerized image processing, the thickness of the Cell Free Layer (CFL) and radial velocity profiles in arterioles were quantified at various levels of systemic Hct. Modeling of radial Hct distributions in arterioles allowed for the estimation of tube Hct (Hct_{tube}), core Hct (Hct_{core}), and the RBC Flux as a function of systemic Hct (Hct_{sys}). Volumetric flow, CFL thickness, and other microvascular hemorheological parameters were found to be sensitive to small variations in hematocrit after hemoconcentration or hemodilution. The variations in volumetric flow, CFL thickness, and related calculated microvascular hemorheological parameters were on average limited to hematocrit between 30% and 60% and plateaued outside this range. However, temporal variations in CFL thickness were found to decrease with hemoconcentration and increase with hemodilution. Calculated wall shear stress was minimized at baseline 45% Hct. Furthermore, both calculated red cell flux and Tube Hct were found to plateau with hemoconcentration. In summary, changes in hemodynamics were

primarily dependent on the changes in viscosity that results from changing the concentration of red cells, while changes in CFL thickness can be attributed to changes in the hydrodynamic forces associated with blood flow and changes in red cell packing efficiency.

2.1 Introduction

Blood is a Non-Newtonian multiphase fluid, consisting of blood cells, plasma, proteins, and electrolytes. Red Blood Cells (RBCs), which constitute nearly 45% of blood volume, are highly deformable biconcave particles of approximately 8 μm diameter. The deformability of RBCs allow them to pass through capillaries much smaller than their characteristic size, giving rise to complex, nonlinear blood rheological properties. Consequently, blood flow in microcirculatory vessels is defined by complex two-phase flow paradigms, in which blood flow is characteristically defined by a central, solid core of packed RBCs and a RBC depleted zone near the vessel wall, known as the RBC Cell Free Layer (CFL). The formation of the CFL in flowing blood is an important hemodynamic feature of the blood flow in the microcirculation, since it corresponds to a low viscosity zone, which acts as a lubricating hydrodynamic layer, reducing resistance to flow between the RBC core and the vessel wall [18, 16]. Previous studies indicate that the thickness of the CFL is proportional to the shear stress of the flowing blood, and its formation is determined by the hematocrit (Hct), the RBC aggregation, and the vessel diameter and geometry [60].

The formation of the CFL and the complex nonlinear rheological properties of blood give rise to phenomena characteristic of blood flow *in vivo*. Two such phenomena, the Fahraeus effect and the Fahraeus-Lindqvist Effect, may be of significant physiological importance in arterioles, where distribution of blood flow and nutrient delivery to tissues occurs. The Fahraeus effect observes that in microcirculatory vessels and small tubes, the tube hematocrit ($\mathrm{Hct_{tube}}$, the concentration of RBCs in the flow stream) is less than the discharge hematocrit ($\mathrm{Hct_{disch}}$, the outflow concentration of RBCs in the tube). Consequently, decreasing vessel diameter results in decreasing $\mathrm{Hct_{tube}}$, as the central RBC core flows at a faster velocity than the average blood

velocity. Recent studies have implicated both the CFL thickness and the Fahraeus effect as important regulators of NO and O2 bioavailability, demonstrating the physiological significance of understanding these two phenomena [56]. Additionally, the Fahraeus Effect allows for a simple mathematical model to relate Hct_{tube} to Hct_{disch}, average cell velocity, and blood vessel diameter as empirically determined by Pries et al. [61, 62]. While both the thickness of the CFL and the Fahraeus effect are known to depend on systemic hematocrit (Hct_{syst}), this relationship and its presence in arterioles has not been studied in detail *in vivo*.

The Fahraeus-Lindqvist Effect observes that blood viscosity changes with tube diameter [32]. This phenomenon is a direct consequence of the dependence of cell free layer thickness on tube diameter, as the CFL provides lubrication for fluid flow. Blood viscosity also depends on hematocrit, as RBCs are the component of blood that contribute most to its viscous behavior [32, 62]. In the context of hemodynamics in the microcirculation, the non-linearity of blood viscosity has implications in fluid shear rate. In particular, the changes in the apparent viscosity of blood due to changing hematocrit, the Fahraeus effect, tube diameter, and CFL thickness, can have effects on the wall shear stress experienced by the endothelial wall. Many studies have correlated effects of blood viscosity on fluid shear stress *in vitro* and *in silico*; however, the clinical implications of increasing blood viscosity on the microcirculatory blood flow *in vivo* have not yet been evaluated [18, 62]. Such studies, if investigated in the context of pathologies associated with changes in hematocrit, including both anemia and polycythemia, might provide useful information and could guide therapeutic interventions.

While a wide range of hematocrit levels is compatible with life, clinically both anemia and polycythemia represent significant problems [63]. As such, understanding the consequences of variations in Hct_{syst} in the microcirculation would aid to better understanding of physiological and pathophysiological consequences of such variations. This study focuses on the effects of hemoconcentration and hemodilution on blood flow in arterioles. Hemoconcentration was induced by exchange transfusion with fresh RBCs in increments of 5%. Utilizing high resolution, high

speed video microscopy and computerized image processing, the thickness of the CFL at various levels of systemic Hct. The relationships obtained from this study in conjunction with information about blood rheological properties and microvascular hemodynamics allow for a more complete understanding of the changes in vascular resistance and CFL thickness in the arteriolar network with hemoconcentration.

2.2 Materials and Methods

2.2.1 Animal Preparation

Animal handling and care procedures were in accordance with the National Institutes of Health Guide for the Care and Use of Laboratory Animals, 2011. The University of California, San Diego Animal Subjects Committee approved the experimental protocol. Twelve Sprague-Dawley rats weighing $140-190$ g were used for intravital microscopy examination; additional animals were used as plasma and RBC donors. Anesthesia was induced using 60 mg/kg i.p of pentobarbital sodium (Nembutal, Lundbeck Inc, Deerfield, IL) and supplemented as needed by i.v. infusion of 20% of the initial dose. Animals were placed on a heating pad to maintain body temperature at 37°C. The jugular vein and femoral artery were catheterized, and a tracheal tube was inserted to support ventilation. Catheters were pre-filled with heparinized saline solution (30 IU/ml).

The rat cremaster muscle was exteriorized as previously described by Baez [27]. The rat was positioned on a plexiglas plate, and the cremaster muscle was secured to a heated platform for viewing. The platform enabled muscle temperature maintenance at 35°C during surgery and the experiment. The muscle was moistened with warm Plasma-Lyte solution (˜37°C) and following surgical preparation, exposure to atmospheric oxygen was prevented by a covering of polyvinyl film (Saran, SC Johnson & Son, Racine, WI).

2.2.2 Blood and plasma Collection

Whole blood was obtained from rat donors, adult male Sprague-Dawley rats (280300 g, n=24). Briefly, rats were anaesthetized, left carotid artery catheter was implanted, and blood was allowed to flow into heparinized tubes (sodium heparin 15 IU/mL). RBCs and plasma were separated by centrifugation (2700 rpm, 7 min). The buffy coat was discarded. RBCs morphology was checked prior to infusion and discarded if cells were crenated.

2.2.3 Isovlemic Exchange Transfusion Protocol

To adjust the Hct_{syst} to the target Hct level the volume of the exchange-transfusion was calculated from the formula, exchange volume $= 0.024V \times \Delta$Hct; where V is equal to the rats blood volume in mL (estimated as 6% of the weight in grams) and ΔHct is the difference between the initial and the target Hct [64]. Packed RBCs or plasma were infused through the jugular vein catheter and an equal volume of blood was withdrawn from the femoral artery, simultaneously, at a rate of 0.3 mL/min to prevent rapid shifts in blood volume.

2.2.4 Experimental Groups

Due to the length of the procedures and to ensure the quality of the microcirculation preparation, animals were divided into two experimental groups, Hemodilution and Hemoconcentration. In both groups, baseline Hct_{syst} was adjusted as needed to 40% to generate a comparable initial Hct for all animals. In the hemodilution group, Hct_{syst} was gradually decreased by 5%, from 40 to 20% Hct. Conversely, Hct_{syst} was gradually increased by 5% in the hemoconcentration group from 40 to 75%. Animals were allowed a 10 min stabilization period following surgery, prior to experimentation.

2.2.5 Systemic Parameters and Blood Measurements

Mean arterial pressure (MAP) and heart rate (HR) were recorded using a pressure transducer connected to the femoral artery catheter using a MP-150 (BIOPAC Systems, Goleta, CA). Blood samples were collected from the femoral artery catheter in heparinized capillary tubes (Fisher Scientific, Pittsburgh, PA) to determine Hctsys by centrifugation (5 min at 8000 rpm, Readacrit; Clay Adams, Division of Becton Dickinson, Parsipanny, NJ). Additionally, blood mixtures were prepared using packed RBCs and fresh plasma to determine blood and plasma viscosities (at 37°C and shear rates of between 50 and 450 sec^{-1}) using a cone-plate viscometer (DV II + Pro, Brookfield, Middleboro, MA, USA).

2.2.6 Intravital Microscope Setup

The experimental setup consisted of an intravital microscope (Olympus-BX51WI), equipped with a 40X objective (LUMPFL-WIR, NA= 0.8; Olympus) and a matching custom long working distance condenser with NA = 0.8 (Thorlabs, Newton, NJ). Additionally, two magnifications of 2X and 1.5X were installed between the objective and the camera to provide a total magnification of 1200X with an equivalent resulting pixel size of 0.125 μm relative to the object plane. Tissue was illuminated with a mercury arc lamp (100 W, Walker Instruments, Scottsdale, AZ). A 400 nm interference filter (Spectra Physics, no. 59820) was placed in the light path to maximize image contrast. Images were recorded with a high-speed video camera (Fastcam 1024 PCI, Photron USA), equipped with a one-megapixel chip. All videos were recorded at 3000 frames per second and the camera shutter speed was increased to obtain the sharpest and clearest image possible.

2.2.7 Computerized Measurement of CFL

The CFL width was measured using high speed and high magnification videos obtained form intravital microscopy of arterioles, which were analyzed off line with a custom image analysis software (see **Supplemental Figure 2.8**). Images were recorded, stabilized [65] and transferred

to an external hard drive. To stabilize the video, images are translated to best align with a template that excludes the blood vessel. Once an image is aligned, it is used as the template to translate the next image, and these steps are repeated throughout the video. The CFL width was determined from the position of the vessel wall and the outer edge of the first red cell encountered, using the changes of intensity along a single video raster line across the vessel and perpendicular to the vessel wall. To position the line exactly perpendicular to the vessel wall, a five-pixel line parallel to the vessel wall at a point of interest was drawn. The edge of the RBC core was determined by Otsus method, which performs a histogram shape-based image threshold reducing a gray-level image to a binary image [66]. The CFL width was measured on both sides of the blood vessel. All the analysis was implemented using ImageJ software (NIH, Bethesda, Maryland) and coordinates of the vessel wall edges were recorded for validation of the automated analysis. In addition to the CFL, the image analysis yielded vessel diameters (D), the RBC core column width. The temporal variation of the measurement (TV) of CFL thickness was calculated as the standard deviation of the CFL during a recording period. The total number of measurements at each Hct ranged from 16000 to 20000.

2.2.8 Experimental Protocol

Imaging for intravital microscopy of straight arteriole (with diameters between 28 - 41 μm) segments (without branches in the field of view), good image quality, and image contrast were selected. Blood sample and microcirculation videos were taken 10 min after the end of the exchange transfusion. Video recording of these arterioles were taken over 1632 frames (3000 fps for 0.54 s). CFL measurements at each Hct level were obtained in each animal from at least one arteriole per animal.

2.2.9 Validation of the Computerized Method

The computerized measurements of the CFL width were compared to manual measurements using ImageJ software along the same raster line as chosen for the computerized method. Computerized and manual measurements were in close agreement in the earlier study at normal levels of Hct_{syst}. To determine whether the computerized method was also reliable over the range studied in this work, comparisons were made over a range of 20 to 75% Hct_{syst}. For this purpose CFL width data were manually obtained from each side of the arteriole every 20th frames from the recorded videos for a period of 0.8 s and compared with the automated measurements. The degree of agreement between the two measurements was determined from Bland & Altman plots and linear regression.

2.2.10 Minimal Measurable CFL width and Random Error Determination

To determine the minimal measurable CFL width and the random errors of the measurement, we used a MetroChip calibration standard (MetroBoost, Santa Clara, CA). Minimal measurable CFL width was established with the line monitor targets of varying pitch. The purpose for this target was to provide lines (1 μm tick) with changing line spacing between 0.1 to 10 μm. Briefly, one line was assumed as the endothelial line and second line as the RBC core line, the space between lines as the CFL, and videos were recorded as described before. The random error that may have been introduced into the measurement by electronic noise and vibrations were calculated by comparing the nominal width with that measured for the computerized and manual methods. Signal-to-noise ratio (SNR) for the imaging setup and the computerized methods was calculated as the reciprocal of the coefficient of variation for various distances of the calibration standard. The Rose criterion (SNR of at least 5), which distinguished image features at 100% certainty, was determined.

2.2.11 Volumetric Flow, RBC Flow, and Plasma Flow

BC Flow and Plasma Flow were approximated to be a fixed percentage of the Volumetric Flow dependent on the systemic hematocrit, as shown below:

$$\begin{aligned} Q_{\text{RBC}} &= \%\ \text{Hct} \times Q_{\text{vol}} \\ Q_{\text{plasma}} &= (1 - \%\ \text{Hct}) \times Q_{\text{vol}} \end{aligned} \tag{2.1}$$

2.2.12 Wall Shear Rate and Wall Shear Stress

Wall Shear Rate (WSR) was approximated as the numerical derivative of the experimentally measured velocity profile, $v_z(r)$ at the vessel wall ($r = R$), where R is the vessel radius. The shear rate is therefore approximated as:

$$\dot{\gamma}(r) = \nabla \vec{v} = \frac{\partial v_z}{\partial r} \tag{2.2}$$

where v_z is the velocity in the axial direction. WSR is thus:

$$\dot{\gamma}_{\text{wall}} = \left.\frac{\partial v_z}{\partial r}\right|_{r=R} \tag{2.3}$$

Error for WSR was calculated using Taylors theorem and is detailed below. Wall Shear Stress (WSS) was approximated utilizing constant plasma viscosity:

$$\tau_{\text{wall}} = \eta_{\text{plasma}} \dot{\gamma}_{\text{wall}} = \eta_{\text{plasma}} \left.\frac{\partial v_z}{\partial r}\right|_{r=R} \tag{2.4}$$

where plasma viscosity, η_{plasma}, was approximated as 1.2 cP.

2.2.13 Error Propagation for Wall Shear Rate and Wall Shear Stress Calculations

Error for both WSR and WSS was approximated using Taylors theorem, as shown below:

$$\begin{aligned} \delta\dot{\gamma}_{\text{wall}} &= \frac{h^4}{30} v_z^{(5)}(R) \\ v_z^{(5)}(R) &= \frac{v_z(R-5h) + 5v_z(R-4h) - 10v_z(R-3h) + 10v_z(R-2h) - 5v_z(R-h) + v_z(R)}{h^5} \end{aligned} \tag{2.5}$$

where $h = \delta r$ is the step size of the velocity profile, $v_z(r)$. Error for WSS is thus determined as follows:

$$\delta\tau_{\text{wall}} = \frac{\partial\tau_{\text{wall}}}{\partial\dot{\gamma}_{\text{wall}}} \delta\dot{\gamma}_{\text{wall}} = \eta_{\text{plasma}} \delta\dot{\gamma}_{\text{wall}} \tag{2.6}$$

Supplemental Figure 2.9 details the shear rate profile determined from the velocity profile used to determine wall shear stress.

2.2.14 RBC Core Area and Cell Free Area

RBC Core Area (A_{core}) and Cell Free Area (CFA) were approximated using a cylindrical cross section:

$$\begin{aligned} A_{\text{core}} &= \pi(R-\delta)^2 \\ \text{CFA} &= \pi R^2 - A_{\text{core}} \end{aligned} \tag{2.7}$$

where δ is the thickness of the cell free layer and R is the vessel radius.

2.2.15 Tube Hematocrit, Core Hematocrit, and RBC Flux

The radial distribution of Hct in a single vessel was approximated as a polynomial with the systemic Hct (Hct_{syst}) as its maximum:

$$\mathrm{Hct}(r) = \begin{cases} \mathrm{Hct}_{\mathrm{syst}} & r = 0 \\ \mathrm{Hct}_{\mathrm{syst}}\left(1 - (\frac{r}{R-\delta})^p\right) & 0 < r \leq (R-\delta) \\ 0 & R-\delta < r \leq R \end{cases} \tag{2.8}$$

where R is the radius of the vessel and δ is the thickness of the CFL. In this model, core hematocrit ($\mathrm{Hct}_{\mathrm{core}}$) is a constant percentage of $\mathrm{Hct}_{\mathrm{syst}}$:

$$\begin{aligned} \mathrm{Hct}_{\mathrm{core}} &= \frac{1}{R-\delta}\int_0^{R-\delta} \mathrm{Hct}_{syst}\left(1 - \left(\frac{r}{R-\delta}\right)^p\right)dr \\ &= \left(1 - \frac{1}{p+1}\right)\mathrm{Hct}_{syst} \end{aligned} \tag{2.9}$$

where p is the polynomial order of the model. For these results, $\mathrm{Hct}_{\mathrm{core}}$ was approximated to be 75% of the systemic hematocrit, translating to a polynomial of order $p = 3$.

Tube hematocrit was approximated as follows:

$$\begin{aligned} \mathrm{Hct}_{\mathrm{tube}} &= \frac{V_{\mathrm{RBC}}}{V_{\mathrm{tot}}} = \frac{1}{\pi R^L}\iint \mathrm{Hct}(r) r dr \\ &= \frac{3}{5}\left(1 - \frac{R}{\delta}\right)^2 \end{aligned} \tag{2.10}$$

RBC Flux was approximated as follows:

$$\Phi_{\mathrm{RBC}} = \frac{Q\mathrm{Hct}_{\mathrm{tube}}}{\pi R^2} = \frac{3Q}{5\pi R^2}\left(1 - \frac{R}{\delta}\right)^2 \tag{2.11}$$

2.2.16 Statistical Analysis

Unless otherwise noted, variables are represented as Mean $\pm$ standard deviation (SD). All statistical calculations were performed with Prism 7 (GraphPad Software, San Diego, CA) and/or

Excel (Microsoft, Redmond, WA). Comparisons between different Hct_{syst} levels were performed using one-way analysis of variance test (ANOVA). Post hoc analyses were performed using the Newman Keuls multiple comparison test. For all statistical tests, $P<0.05$ was accepted as statistically significant. All animals passed the Grubbs test, ensuring that all the measured values at baseline were within a similar population ($P < 0.05$).

2.3 Results

A total of twelve animals were entered into the study, two or three arteries were selected in each animal. After application of the systemic and vessel reactivity inclusion criteria, data from thirty-two (n = 32; 18 in the hemodilution and 14 in the hemoconcentration groups) arterioles were included in the results. For all results presented, baseline Hct was 45%. There were no significant differences in the systemic or microhemodynamics parameters at baseline.

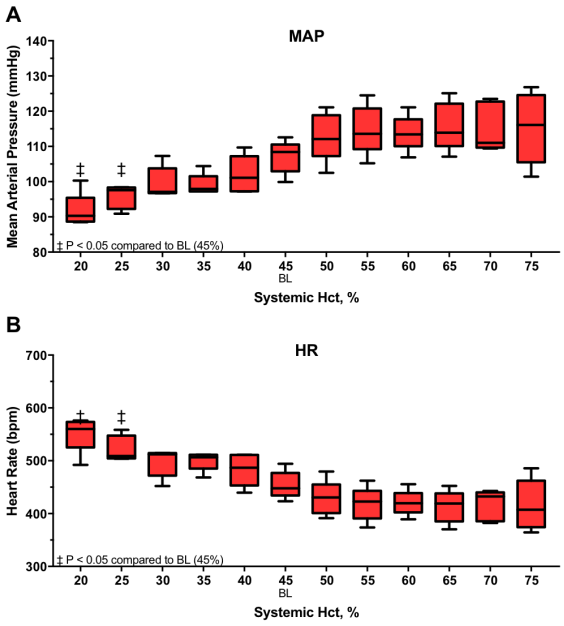

Figure 2.1: Hemodynamic Changes after Hemodilution and Hemoconcentration: **(A)** Mean Arterial Pressure (MAP). MAP was found to increase with hemoconcentration and decrease with hemodilution. **(B)** Heart Rate (HR). HR was found to increase with hemodilution and decrease with hemoconcentration

2.3.1 Systemic Parameters

Mean arterial pressure and HR after hemodilution and hemoconcentration are presented in **Figures 2.1A** and **2.1B**. MAP was observed to increase with hemoconcentration and decrease with hemodilution. However, changes in MAP were found to plateau at Hct $> 55\%$. HR was observed to decrease with hemoconcentration and increase with hemodilution. There were statistically significant differences in both MAP and HR from baseline (45% Hct) compared to 20 and 25% Hct_{syst}.

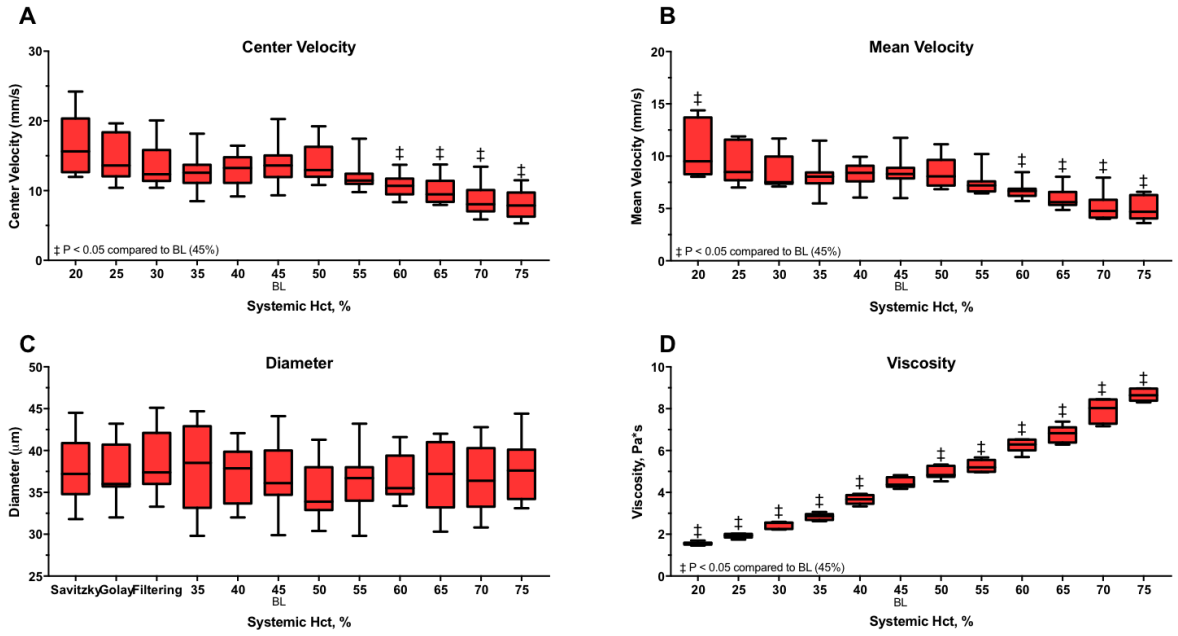

Figure 2.2: Changes in Velocity, Diameter, and Blood Viscosity after Hemodilution and Hemoconcentration: **(A)** Center Velocity. Center velocity was found to decrease with hemoconcentration and increase with hemodilution. **(B)** Mean Velocity. Mean velocity was found to decrease with hemoconcentration and increase with hemodilution. **(C)** Diameter. No significant changes in diameter were observed with hemoconcentration or hemodilution. **(D)** Viscosity. Viscosity was found to linearly increase with Hct variations.

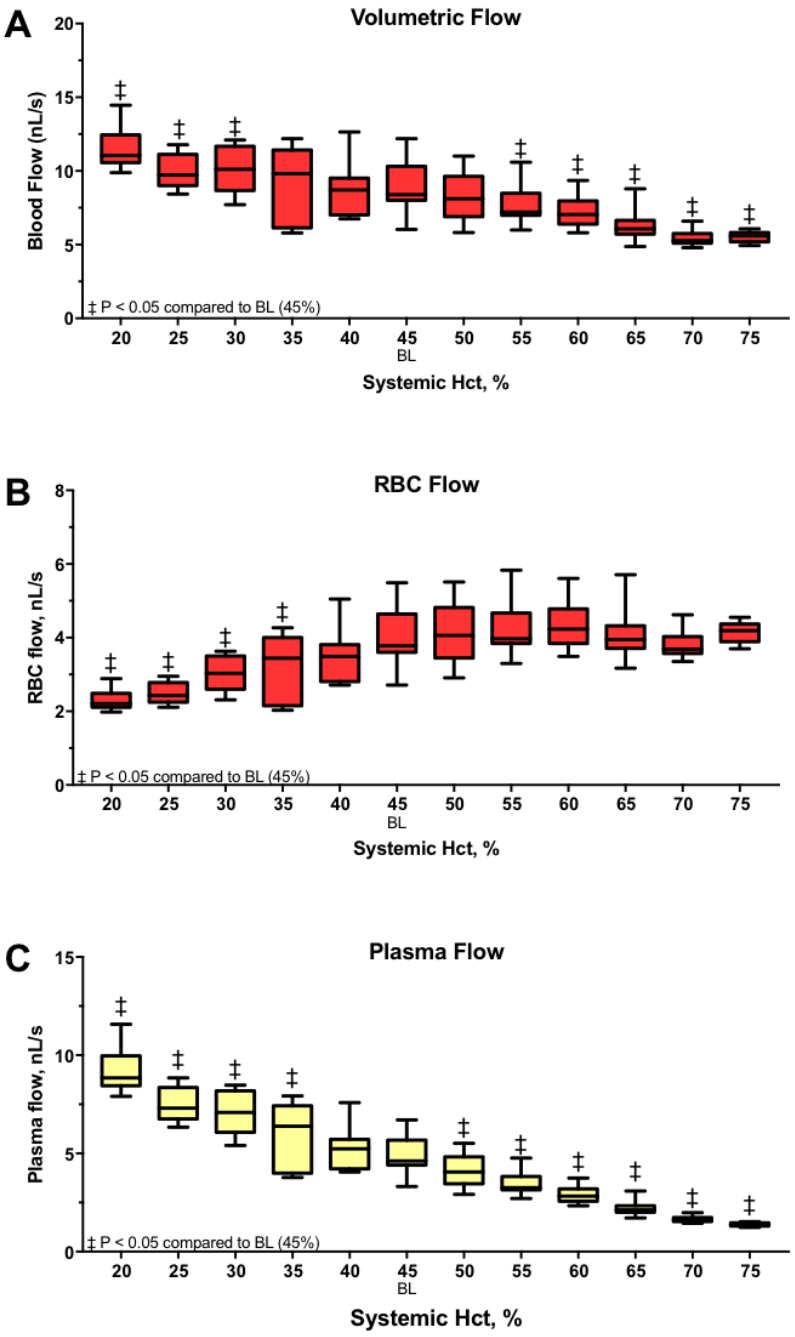

Figure 2.3: Changes in Flow after Hemodilution and Hemoconcentration: **(A)** Volumetric Flow. Volumetric was found to increase with hemodilution and decrease with hemoconcentration. **(B)** RBC Flow. RBC Flow was estimated as the product of % Hct and Volumetric Flow. RBC Flow was found to decrease with hemodilution and increase with hemoconcentration. **(C)** Plasma Flow. Plasma flow, estimated as the difference between volumetric flow and RBC flow, increased with hemodilution and decrease with hemoconcentration.

2.3.2 Microhemodynamic Parameters

Centerline velocity (V_{center}) and mean velocity (V_{mean}) were found to be statistically lower from baseline (45% Hct) at high Hct ($> 60\%$) (**Figures 2.2A, 2.2B**). Additionally, V_{mean} was statistically higher compared to that at baseline (45% Hct) at Hct 20%. Minimal changes were observed in both centerline and mean velocity with hemodilution; however, the majority of changes in both these parameters were observed after hemoconcentration, as a consequence of the increasing significance of viscosity. No statistically significant differences in diameter were observed at all Hct compared to baseline (**Figure 2.2C**). Blood viscosity was found to vary linearly with Hct with a slope statistically significant from 0 (**Figure 2.2D**), as RBCs contribute most to the non-linear viscous behavior of blood.

2.3.3 Volumetric Flow, RBC Flow, and Plasma Flow

RBC Flow (Q_{RBC}) and Plasma Flow (Q_{plasma}) were approximated as a fixed percentage of volumetric flow (Q) at a given Hct. Q was found to statistically deviate ($P < 0.05$) from baseline (45% Hct) at low Hct (<30%) and high Hct (>55%) and was found to vary linearly with Hct with a slope statistically significant from 0 (**Figure 2.3A**). Q_{RBC} was found to be statistically lower than that at baseline for all Hct $< 35\%$ but not for higher Hct (**Figure 2.3B**). Q_{plasma} was found to be statistically different from that at baseline at Hct $< 35\%$ and Hct $> 50\%$ (**Figure 2.3C**).

2.3.4 Wall Shear Rate (WSR) and Wall Shear Stress (WSS)

WSR and WSS were both found to be statistically different from baseline Hct (45% Hct) at 50% Hct (**Figures 2.4A, 2.4B**). No other statistical differences were observed. WSR and WSS were both observed to minimized at baseline (45% Hct). Furthermore, WSR and WSS increased with both hemoconcentration and hemodilution, indicating that both changes in apparent viscosity and changes in CFL thickness influence these parameters. WSR and WSS were also found to be more sensitive to hemoconcentration as opposed to hemodilution. Additionally, the variance of

the WSR and WSS decreased with Hct, likely due to the decrease in the temporal variation (TV) of the CFL thickness that was observed with increasing Hct.

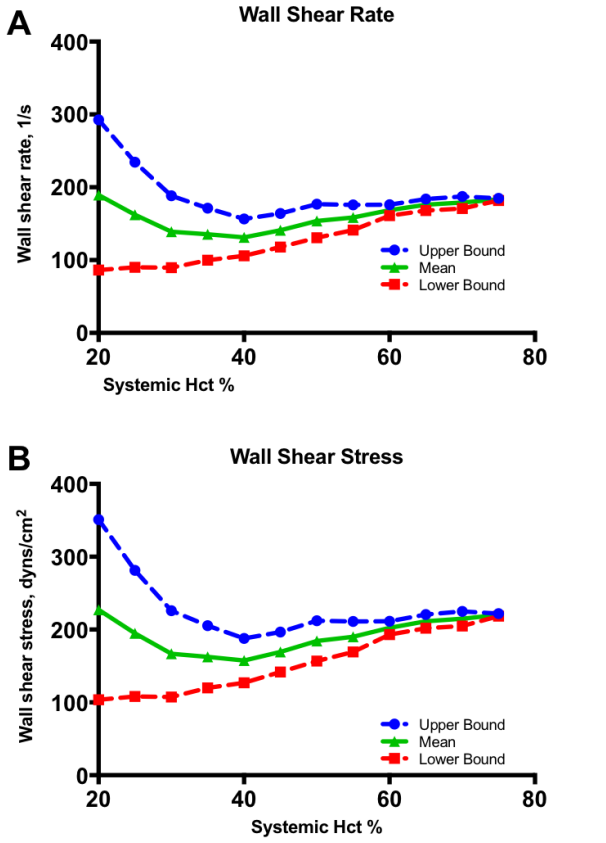

Figure 2.4: Changes in Wall Shear Rate (WSR) and Wall Shear Stress (WSS) after Hemodilution and Hemoconcentration: **(A)** Wall Shear Rate. WSR was estimated as the radial gradient of velocity profiles. The upper and lower limits of velocity profiles were obtained from normalized cross-correlation, resulting in upper and lower limits for WSR. WSR was observed to be minimized at baseline Hct (45%) and increased with both hemoconcentration and hemodilution. **(B)** Wall Shear Stress. WSS was estimated as the product of WSR and plasma viscosity, which was assumed to be constant. Therefore, WSS followed the same trend as WSR and was minimized at baseline Hct (45%) and increased with both hemoconcentration and hemodilution.

2.3.5 Cell Free Layer (CFL) Thickness, RBC Core Area, and Cell Free Area

The thickness of the CFL and the Cell Free Area were found to be statistically different from that at baseline at all Hct (**Figures 2.5A, 2.5C**). Additionally, the temporal variation of CFL thickness measurements was found to increase with hemodilution and decrease with hemocon-

centration. Changes in CFL thickness plateaued above 60% Hct due to volumetric constraints. Conversely, changes in CFL thickness plateaued below 30% Hct due to limitations imposed by the hydrodynamic forces present. The RBC Core Area was found to be statistically different from that at baseline for all Hct except at 55% Hct, where no differences were observed (**Figure 2.5B**). As expected, changes in RBC Core Area inversed correlated with those observed for CFL thickness/Cell Free Area after hemoconcentration and hemodilution.

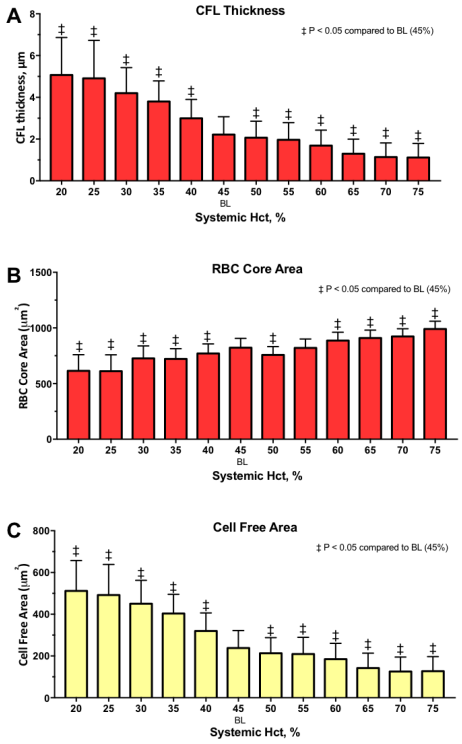

Figure 2.5: Changes in Cell Free Layer Thickness, RBC Core Area, and Cell Free Area after Hemodilution and Hemoconcentration: **(A)** CFL Thickness. CFL thickness was measured using high speed and high magnification videos obtained form intravital microscopy of arterioles, which were analyzed offline with custom image analysis software. CFL thickness was found to increase with hemodilution and decrease with hemoconcentration. **(B)** RBC Core Area. RBC Core Area was calculated as $A_{\text{core}} = \pi(R-\delta)^2$ where R is the radius of the tube and δ is CFL thickness. RBC Core area was observed to decrease with hemodilution and increase with hemoconcentration. **(C)** Cell Free Area. Cell Free Area was calculated as the difference between tube cross sectional area and RBC Core Area. Consequently, Cell Free Area followed the same trend as CFL thickness.

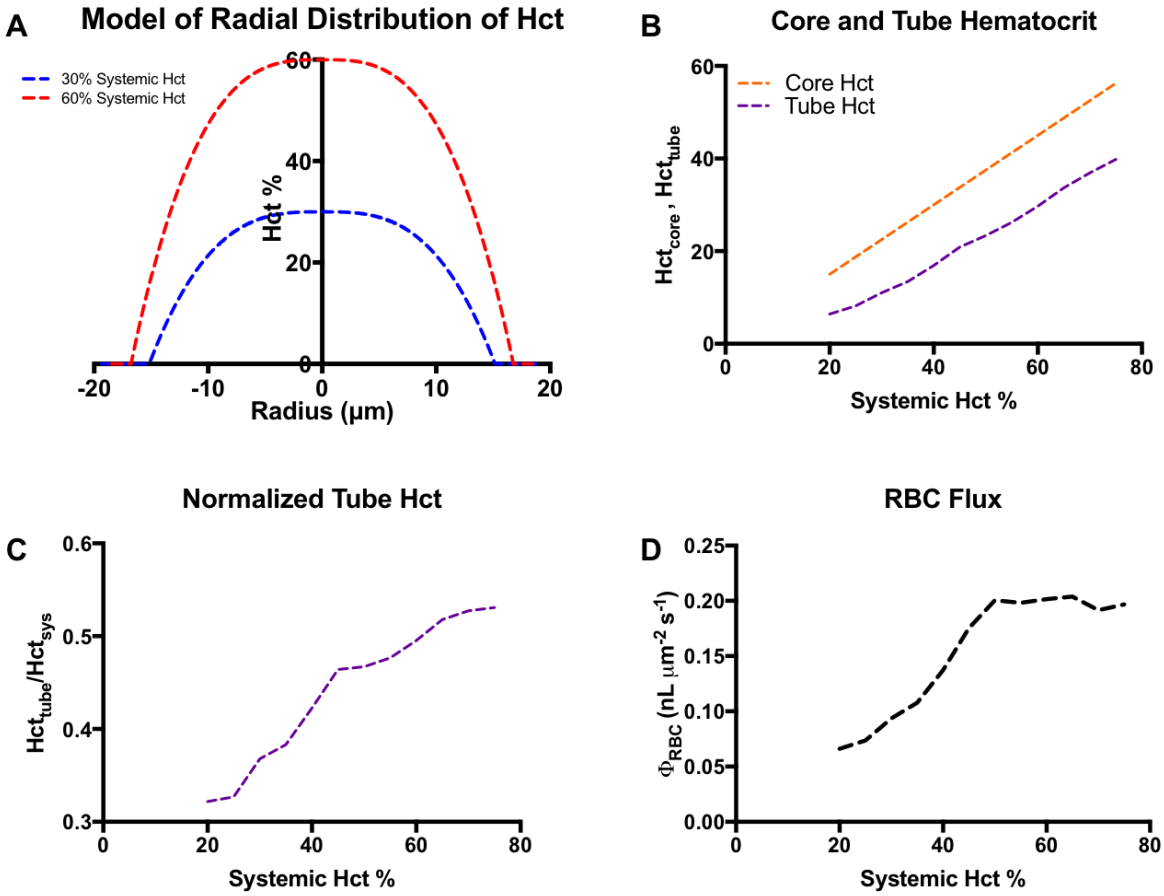

Figure 2.6: Radial Hct, Core Hct, Tube Hct, and RBC Flux after Hemodilution and Hemoconcentration: **(A)** Radial Hct. Radial Hct for 30% and 60% systemic Hct are shown. Distributions followed the model $\text{Hct}(r) = Ar^p + \text{Hct}_{\text{syst}}$ where A was calculated from the model assuming 0% Hct at the CFL. As CFL is a function of Hct, hemoconcentration resulted in broadening of the distribution. **(B)** Core Hct and Tube Hct. As a consequence of the polynomial model, Core Hct is a fixed proportion of systemic Hct. Both Tube and Core Hct were found to increase with systemic Hct, as expected. **(C)** Normalized Tube Hct. Normalization of Tube Hct with respect to systemic Hct revealed decrease in the rate of change of Tube Hct with respect to systemic Hct after hemoconcentration. **(D)** RBC Flux. RBC Flux was calculated using the Tube Hct and was observed to plateau with hemoconcentration and decrease with hemodilution.

2.3.6 Core Hematocrit, Tube Hematocrit, and RBC Flux

Figure 2.6A demonstrates the approximation of the radial distribution of Hct of polynomial order 3 used to approximate the core and tube hematocrit. Core hematocrit and tube hematocrit were observed to linearly increase with systemic Hct (**Figure 2.6B**). When tube Hct was nor-

malized with respect to systemic Hct, normalized tube hematocrit was found to vary linearly with core hematocrit at a slower rate at Hct $> 45\%$ (**Figure 2.6C**). RBC Flux was found to vary linearly with systemic Hct at Hct $< 45\%$ and found to plateau at Hct $> 45\%$ (**Figure 2.6D**). Qualitatively, changes in both Tube Hct and RBC Flux decreased with hemoconcentration. In both these cases, this a consequence of the increasing significance of viscous forces due to the increasing systemic Hct.

2.4 Discussion

The principal finding of this study are that volumetric flow, the CFL thickness, and other microvascular hemorheological parameters were found to be very sensitive to small variations in hematocrit after hemoconcentration or hemodilution. The blood volumes were maintained as near to normal as possible with only changes in hematocrit. These results confirm early studies, which postulated the optimal hematocrit hypothesis, originally based on studies with mammals [67, 68], suggesting a balance between the inadequate carrying capacity resulting from abnormally low hematocrit (anemia) and the viscosity-induced decreases in blood flow that result from abnormally high hematocrit values (polycythemia). Isovolemic alterations of hematocrit within a certain range lead to an essentially constant rate of O_2 transport, as the opposing effects due to changes in oxygen-carrying capacity and blood viscosity are balanced with each other. The range of this optimum hematocrit, however, shows considerable variations [67, 68]. The current study found that the variations in the regional responses of vascular hindrance to hematocrit variations are restricted to a limited range within the normal hematocrit value.

The variations in volumetric flow, CFL thickness, and related calculated microvascular hemorheological parameters were on average limited to hematocrit between 30% and 60% and plateaued outside this range. Volumetric flow was found to statistically increase by 30% with hemodilution and decrease by 40% with hemoconcentration. As mentioned above, these changes were limited to hematocrit between 30% and 60%; outside this range, volumetric flow plateaued.

A similar phenomenon was observed for plasma flow. These results are representative of the effects of changing hematocrit on blood viscosity. Increasing hematocrit increases blood viscosity, as RBCs are the component of blood that contributes to its viscous and non-Newtonian behavior. As a result, hemodynamics of blood with a high hematocrit is dominated by its viscous forces and has a low Reynolds number. Assuming relatively local pressure gradients, blood with high hematocrit will have a much lower velocity and thus less volumetric flow than blood with normal hematocrit, because the energy of the pressure gradients driving flow is dissipated by the viscous forces present. Likewise, blood with low hematocrit dissipates less energy for a given pressure gradient, resulting in a higher velocity and a larger volumetric flow, as observed. Unlike volumetric flow, however, RBC flow, which was estimated as the % Hct multiplied by the volumetric flow, was found to only statistically decrease with hemodilution by a maximum of 42%. No changes were observed with hemoconcentration. These results are best justified by the two counteracting forces that influence the mass flux of RBCs: volumetric flow and hematocrit. As discussed above, increasing hematocrit simultaneously increases blood viscosity, thus decreasing volumetric flow. The increase in the concentration of RBCs at high hematocrit is therefore counteracted by the decrease in volumetric flow. Because RBC flow plateaued with hemoconcentration, thus the decrease in volumetric flow dominates the increase in RBC concentration after hemoconcentration.

The CFL thickness increased by a maximum of 129% after hemodilution and decreased by 49% after hemoconcentration. Cell free area, which is proportional to the CFL thickness, followed a similar pattern. RBC Core area, estimated as the vessel cross sectional area containing the flowing RBCs excluding the cell free area, followed the inverse trend, decreasing by a maximum of 26% after hemodilution and increasing by a maximum of 20% after hemoconcentration. Changes in all three of these parameters were limited to between 30% and 60% hematocrit and plateaued outside this range. The variance in the CFL thickness was also to found be statistically greater after hemodilution when compared to hemoconcentration. These results are best analyzed

in the context of the hydrodynamic forces that affect hemodynamics of blood flow in arterioles in the microcirculation. Blood flow in the microvasculature has been traditionally modeled as a two-phase fluid, defined by the red cell core and the plasma in the CFL. In this schema, plasma in the CFL acts as a lubrication layer, decreasing the net viscosity. As a result, variations in the CFL from hemoconcentration and hemodilution result in changes the behavior of flow in the microcirculation. In this model, two counteracting forces affect blood flow: 1) hydrodynamic fluid forces associated with the vessel wall and the endothelial glycocalyx, and 2) red cell packing efficiency. At low hematocrit, blood flow is influenced primarily by the first of these forces (i.e. the hydrodynamic forces associated with the vessel wall and the endothelial glycocalyx). Because the CFL thickness is proportional to the magnitude of these hydrodynamic forces, blood flow with lower hematocrit will have a much thicker CFL, as observed. The variance of the CFL thickness was also found to increase with hemodilution and decrease with hemoconcentration. This is a consequence of both the increase in hydrodynamic forces associated with the increase in volumetric flow and the increase in the degrees of motion for any given red cell. Therefore, while flow in the red cell core remains relatively laminar, during low hematocrit, flow in the cell free layer becomes more chaotic (i.e. the Reynolds number increases). Conversely, at high hematocrit, blood flow is dominated by the RBC packing efficiency. Because RBCs have a finite volume and are negatively charged, packing of RBCs in a tube is limited by the volume in which they reside. As a result, the CFL at high hematocrit is the theoretical minimum CFL that must exist due the presence of the endothelial glycocalyx, a complex network of glycoproteins, proteoglycans, and glycosaminoglycans that lines the vascular endothelial cells facing the lumen of blood vessels.

Both the variations in volumetric flow and CFL thickness from hemoconcentration and hemodilution contribute to changes in tube and core Hct observed (i.e. the Fahraeus effect) [69, 70]. In the case of the analysis presented here, a polynomial model was used to model Hct as a function of tube radius, with the systemic Hct approximating the Hct at the tube center (**Figure 2.6A**). One major limitation of this model, however, is that the normalized core Hct is a

fixed percentage of the systemic Hct (i.e. the core Hct is linearly proportional to the systemic Hct) (**Figure 2.6B**). In accordance with the literature, a polynomial of order 3 was used to model the radial Hct distribution, such that the core Hct was fixed at 75% the systemic Hct [71]. **Figure 2.6C** presents an estimation of the normalized Hct_{tube} calculated using this model, the vessel diameter, and the CFL thickness. At hematocrit $> 45\%$, it is clear Hct_{syst} has limited influence of the change in Hct_{tube}, because Hct_{disch} is always less than Hct_{tube}; thus, it can be assumed that hemoconcentration does not increase Hct_{tube} as arteriole size decreases. The effects of hemoconcentration on O_2 delivery are better analyzed in the context of RBC flux [72]. n the case of this model, RBC flux can be approximated from the calculated Hct_{tube} and the measured volumetric flow rate. As a result, RBC flux is dependent on Hct_{syst}, tube diameter, CFL thickness, and volumetric flow rate. As presented in **Figure 2.6D**, it is evident that at hematocrit $> 45\%$ (i.e. baseline), RBC Flux does not change. Therefore, hemoconcentration provides little benefit regarding transport of red cells in the microcirculation [73]. Additionally, because hemoconcentration results in an increase in the viscosity of blood, both volumetric flow rate and convective flux decrease [72, 73]. As oxygen delivery is dependent on both the mass flux of RBCs and the convective flux of the fluid, oxygen delivery is likely impaired during hemoconcentration. Thus, the decrease in convective RBC flux due to decreased volumetric indicate that hemoconcentration impairs oxygen delivery.

Variations in the CFL thickness that result from hemoconcentration and hemodilution have implications regarding vascular wall shear rate and wall shear stress [60]. In this study, wall shear rate was estimated as the spatial gradient of the radial velocity profile. Wall shear stress was estimated as the product of the wall shear rate and plasma viscosity, as the plasma in the cell free layer most contributes to shear stress on the endothelial wall of the arteriole. This estimate, however, fails to account for changes in apparent viscosity that result from changing hematocrit, tube diameter, and shear rate. During hemoconcentration and hemodilution, however, the thickness of the CFL varies due to variations in the hydrodynamic forces associated with

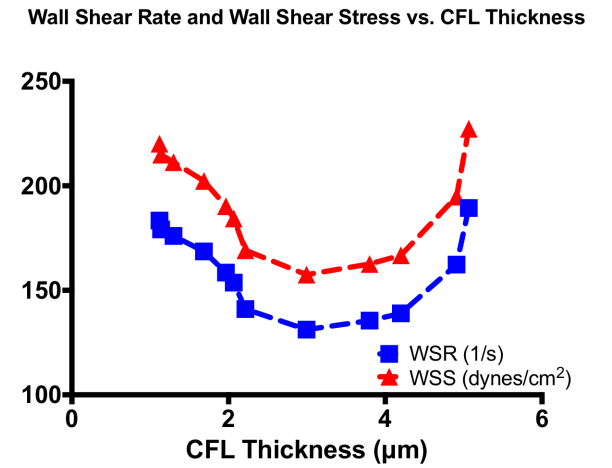

Figure 2.7: Wall Shear Rate and Wall Shear Stress vs. CFL Thickness: WSR and WSS were both analyzed as a function of CFL thickness, as CFL thickness is a function of systemic Hct. Both WSR and WSS were observed to be minimized at the baseline CFL thickness. Variations in CFL thickness resulted in an increase in both WSR and WSS. Additionally, changes in WSR and WSS increased more rapidly as CFL thickness increased.

vessel wall that result from changing hematocrit. Consequently, vascular wall shear rate and wall shear stress both change with hemoconcentration and hemodilution. Analysis of microvascular wall shear rate and wall shear stress as function of the Hctsys and the thickness of the CFL shows that both wall shear rate and wall shear stress are lowest at baseline Hct (45%), as presented in **Figure 2.7**. Both hemoconcentration and hemodilution, therefore, increased the microvascular wall shear stress. During hemodilution, the increase in volumetric flow rate coupled with the increase in the degrees of freedom of motion of RBCs increased the vascular wall shear stress. During hemoconcentration, however, the increase in vascular wall shear stress results from the decrease in the thickness of the CFL. Decreasing the thickness of the CFL, dr, results in an increase in the radial velocity gradient, ∇v, thus increasing wall shear rate and wall shear stress.

Variations in the CFL thickness that result from hemodilution and hemoconcentration also have implications in NO and O_2 bioavailability. As presented in **Figure 7**, variations in CFL thickness result in increased wall shear stress and thus increased NO production by means of endothelial nitric oxide synthase (eNOS). Diffusion of NO towards the lumen limits bioavailability

of NO as NO can undergo many biological reactions with oxygen and hemoglobin. In the case of hemodilution, the increase in convective flux limits the amount of oxygen present in the CFL. As a result, bioavailability of NO is relatively unaffected. However, in the case of hemoconcentration, the decrease in convective flux due to the increase in viscosity increases the amount of O_2 present locally. Additionally, the decrease in CFL thickness increases diffusion of NO and O_2. Consequently, reactions between NO and O_2 become more frequent, limiting bioavailability of both NO and O_2. Changes in NO and O_2 bioavailability are expected to be significant during hemoconcentration. With regard to diffusion of NO predicted from the results, the results presented here are in agreement with those calculated by Lamkin-Kennard *in silico*; however, the future studies should investigate the clinical implications of the predicted changes in both NO and O_2 predicted here [56]. The contribution of each of the RBC-associated factors (unstirred layer versus an intrinsic membrane barrier) to reduce NO scavenging in blood is the subject of some debate [74]. Rapid mixing of NO with RBCs directly measures the rate of NO uptake but both the unstirred layer and intrinsic membrane barrier could potentially be responsible for the slow NO uptake observed in these measurements [75]. Rapid mixing of NO with RBCs directly measures the rate of NO uptake but both the unstirred layer and intrinsic membrane barrier could potentially be responsible for the slow NO uptake observed in these measurements [76]. These changes were found to be associated with a decrease in tissue perfusion and were implicated in the tissue damage following injury [77].

The results from this study have clinical implications on the changes in hemodynamics and cardiovascular dependent parameters in the context of pathophysiologies associated with changes in hematocrit, namely anemia and polycythemia. An elevated blood viscosity is associated with polycythemia, which is implicated in many disorders, including vascular disease and myocardial infarction. These changes were found to be associated with a decrease in tissue perfusion and were implicated in the tissue damage following injury. Epidemiological evidence indicates that patients with high hematocrit are prone to limited perfusion, vascular occlusive disease, and

impaired collateral perfusion and penumbral salvage [78].

In cases of low hematocrit, the adverse rheological effects of hemorrhage could be reversed by the infusion of a plasma expander to preserve blood volume without the need for transfusion. Introduction of a plasma expander reduces hematocrit and, unless its fluid viscosity is like that of blood, the apparent viscosity of blood is reduced. The resulting hemodilution has long been regarded as beneficial as oxygen carrying capacity is minimally increased despite the decrease in hematocrit. The limit of hemodilution (or plasma expansion) is reached when perfusion and oxygen delivery no longer maintain tissue metabolism, a point termed the transfusion trigger. At this point, restoration of blood oxygen carrying capacity is considered necessary. The relevance of maintaining adequate FCD is not fully appreciated in medicine, despite capillary perfusion being linked to tissue oxygen delivery (DO_2), as maintenance of adequate tissue PO_2 is the hallmark of normal tissue function. However, systematic studies of DO_2 to the tissue by the microcirculation show that most of the oxygen in blood is delivered to the tissue by arterioles (skeletal muscle at rest and connective tissue) prior to blood arriving at the capillaries [79]. While capillaries may not be the primary conduits for tissue oxygen delivery, maintaining normal levels of FCD is required to extract products of metabolism from the tissue, which would otherwise create toxic local conditions. The products of metabolism (excluding protons) such as lactate are less diffusible than oxygen, and their clearance requires a functional capillary network.

This study demonstrates effects on volumetric flow and CFL thickness in the context of hemodilution and hemoconcentration utilizing *in vivo* models. Changes in volumetric flow were primarily dependent on the changes in viscosity that results from changing the concentration of red cells. However, changes in CFL thickness can be attributed to changes in the hydrodynamic forces associated with blood flow and changes in red cell packing efficiency. In addition, while hemodilution decreased oxygen delivery by decreasing the mass flux of red cells, increasing hematocrit resulted in little variation in red cell flux, primarily because the change in viscosity counteracted in the increase in mass flux. The viscosity measurements presented have little

significance to the apparent viscosity observed, as the linear trend between viscosity and hematocrit is observed *in vitro* and not *in vivo*. Future studies should aim to estimate the apparent viscosity utilizing the dynamics of blood flow *in vivo*. Additionally, exchanges to obtain the target hematocrit were isovolemic and not normovolemic. As a result, it is not possible to distinguish effects due to changes in flow dynamics and effects due to changes in volume due to changes in colloidal osmotic pressure. Future studies should aim to distinguish between those effects utilizing *in vivo* models.

2.5 Conclusion

These results demonstrate that volumetric flow, the CFL thickness, and other microvascular hemorheological parameters were found to be sensitive to small variations in hematocrit from the hemoconcentration or hemodilution. Many of these changes were limited to a narrow range Hct range (30-60%) due to the two opposing forces that influence hemodynamics in the microcirculation, namely hydrodynamic forces associated with the vessel wall and the Fahraeus-Lindqvist effect. In addition, mathematical estimation of the tube Hct and RBC flux revealed that increasing hematocrit had minimal effect on RBC Flux and oxygen delivery. Future studies should aim to estimate the apparent viscosity utilizing the dynamics of blood flow *in vivo*.

2.6 Supplemental Information

Supplemental Figures are shown below:

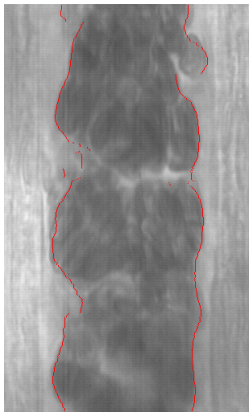

Figure 2.8: Computerized Measurement of CFL: The boundary of the CFL was determined utilizing a custom image processing scheme implemented via Java in ImageJ. A modified Canny Edge Detector, designed as a 2D Sobel Filter convolved with a Gaussian blur, was run across the image, followed by a rectangular morphological processor. Following edge identification, the edge was smoothed using a 1D smoothing filter.

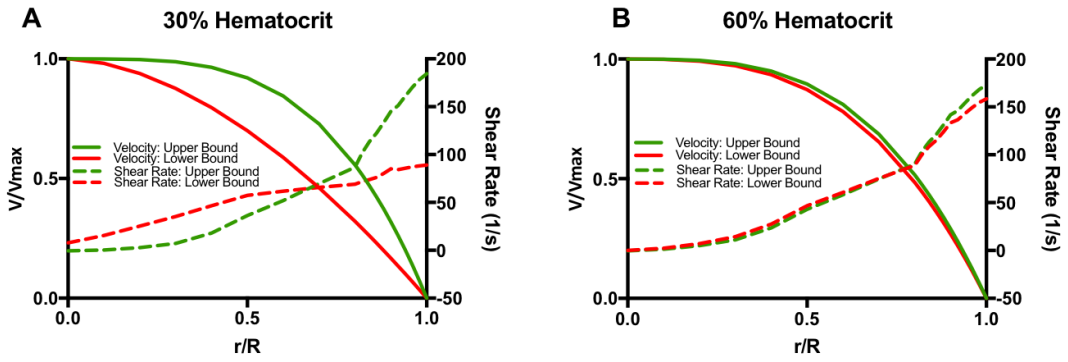

Figure 2.9: Calculation of Shear Rate: Shear rate was estimated as the radial gradient velocity. Calculations for (A) 30% Hematocrit and (B) 60% Hematocrit are shown here. Shear rate at $r/R = 1$ is the Wall Shear Rate (WSR).

Chapter 2, in full, is currently being prepared for submission for publication of the material as it appears in Implications of Systemic Hematocrit on Microvascular Hemodynamics, From Blood Flow to the Radial Distribution of Red Cells and Plasma in Microvessels 2018. Jani, V. P., Yalcin, O., Lucas, A., Williams, A. T., Johnson, P. C., & Cabrales, P. The thesis author was the primary investigator and author of this material.

Chapter 3

A Computer Vision Algorithm to Automatically Detect Microvessel Diameter in High Speed Intravital Microscopy Videos

3.1 Introduction

With the advent of deep learning and its implications in image processing, it becomes useful to analyze the data obtained from in vivo microcirculatory studies from high-speed intravital microscopy videos of window chamber models. These types of analyses provide methods for obtaining high spatial and temporal resolution data of microvascular hemodynamic parameters, like velocity and shear rate. However, deep learning implementations of image analysis are severely limited due to the large number of videos required for training. The algorithm presented here presents an improved computer vision and image processing technique developed to analyze the spatial variations in the arteriolar cell free layer within a single vessel. Compared to other methods, which generally exploit binary thresholding via Otsu's method, the method presented here is more robust and less sensitive to variability in image acquisition [29]. Briefly, the algorithm developed is a modified Canny Edge Detector coupled with a morphological image processor. Morphological image processing has the advantage that cellular artifacts present in the images to be analyzed can be eliminated.

As demonstrated in **Figure 3.1**, the image processing algorithm employed utilized serial image

enhancements to ultimately enhance the edges of the vessel for automatic diameter detection. Utilizing a Gaussian Blur, followed by edge enhancement via application of the Sobel operator, the edges were identified. In order to eliminate cellular artifacts and thus increase the robustness of the algorithm, morphological processing was utilized. In this case, a rectangular morphological element was utilized in order to eliminate circular artifacts. From the morphologically processed image, the user has the option of determining whether or not to obtain the average diameter of the vessel, or a map of the vessel. While both utilize the same algorithm, in which the relative maxima closes to the center of the blood vessel is assumed to be the edge, the average diameter is calculated by performing the algorithm on the the mean intensity of the image, while the diameter map is performed on a row by row basis.

The algorithm was then applied to 2 different high speed intravital microscopy videos obtained from two different animal models, namely the rat cremaster model and the hamster dorsal skinfold window chamber, and was able to successfully detect the diameter and cell free layer of the blood vessel with little modification. The diameter detection algorithm presented here improves upon current methods of edge detection and provides a novel means to analyze spatial and temporal variations in diameter and arteriolar cell free layer thickness.

3.2 Materials and Methods

3.2.1 Animal Care and Handling

Animal handling and care procedures were in accordance with the National Institutes of Health Guide for the Care and Use of Laboratory Animals, 2011. The University of California, San Diego Animal Subjects Committee approved the experimental protocol. For microcirculation videos derived from the rat cremaster muscle, the muscle was exteriorized as previously described by Baez [27]. The rat was positioned on a plexiglas plate, and the cremaster muscle was secured to a heated platform for viewing. The platform enabled muscle temperature maintenance at 35°C

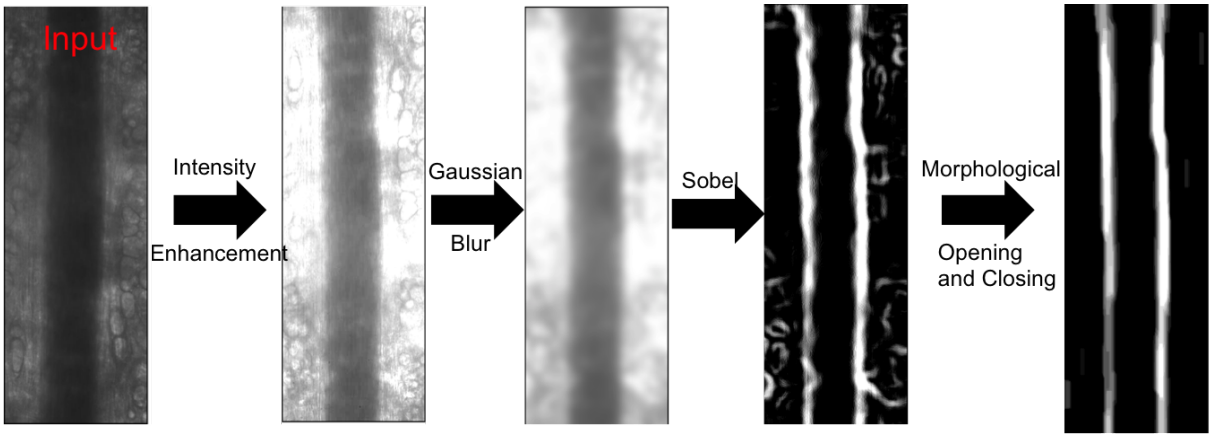

Figure 3.1: Overview of Algorithm to Automatically Detect Microvessel Diameter: Enhancement of the image involved intensity thresholding, followed by a Gaussian blur with radius 9. On smoothened image, a sobel gradient filter was applied to enhance the images. Morphological processing with a rectangular structural element was then utilized in order to eliminate cellular artifacts. After image processing, the relative maxima closed to the center of the vessel were assumed to be the edges of the vessel, from which diameter was calculated.

during surgery and the experiment. The muscle was moistened with warm Plasma-Lyte solution (˜37°C) and following surgical preparation, exposure to atmospheric oxygen was prevented by a covering of polyvinyl film (Saran, SC Johnson & Son, Racine, WI).

For videos obtained from the dorsal skinfold window chamber model in golden syrian hamsters, in vivo studies were performed in 5466 g male Golden Syrian Hamsters (Charles River Laboratories, Boston, MA) fitted with a dorsal skinfold window chamber. The hamster window chamber model is widely used for microvascular studies in the unanesthetized state (complete surgical technique is described in the literature) [80]. Arterial and venous catheters filled with a heparinized saline solution (30 IU/ml) were implanted into the carotid and jugular vessels. Catheters were tunneled under the skin, exteriorized at the dorsal side of the neck, and securely attached to the window frame. Animal handling and care followed the NIH Guide for the Care and Use of Laboratory Animals. The experimental protocol was approved by UC San Diego Animal Care and Use Committee (IACUC).

3.2.2 Intravital Microscopy Setup

The experimental setup consisted of an intravital microscope (Olympus-BX51WI), equipped with a 40X objective (LUMPFL-WIR, NA= 0.8; Olympus) and a matching custom long working distance condenser with NA = 0.8 (Thorlabs, Newton, NJ). Additionally, two magnifications of 2X and 1.5X were installed between the objective and the camera to provide a total magnification of 1200X with an equivalent resulting pixel size of 0.125 μm relative to the object plane. Tissue was illuminated with a mercury arc lamp (100 W, Walker Instruments, Scottsdale, AZ). A 400 nm interference filter (Spectra Physics, no. 59820) was placed in the light path to maximize image contrast. Images were recorded with a high-speed video camera (Fastcam 1024 PCI, Photron USA), equipped with a one-megapixel chip. All videos were recorded at 2000 frames per second and the camera shutter speed was increased to obtain the sharpest and clearest image possible.

3.2.3 Intensity Enhancement

Intensity enhancement involves linearly scaling intensities within a specified range between 0 and 255. Let the range $I \in [I_{min}, I_{max}]$ be the range of intensity enhancement in this algorithm, and let I_{ijt} be the intensity of a pixel in row $i \in [0, M]$, column $j \in [0, N]$, and frame $t \in [0, T]$. Intensity enhancement was performed as follows:

$$I'_{ijt} = \begin{cases} 0 & I_{ijt} < I_{min} \\ \frac{255}{I_{max} - I_{min}} I_{ijt} + \left(255 - \frac{255 I_{max}}{I_{max} - I_{min}}\right) & I_{min} \leq I_{ijt} \leq I_{max} \\ 255 & I_{ijt} > I_{max} \end{cases} \tag{3.1}$$

For this algorithm, I_{min} and I_{max} were empirically determined to be 0 and $\bar{I} + \sigma_I$, respectively, where $\bar{I}$ is the mean intensity of the image and σ_I is standard deviation.

3.2.4 Gaussian Blur

Following intensity enhancement convolution was applied to the image. Let σ be the user-defined variance of the convolution, and the kernel of convolution be of size 3σ. In 2 dimensions, the Gaussian takes the form:

$$G(x,y) = \frac{1}{2\pi\sigma^2} e^{-\frac{x^2+y^2}{2\sigma^2}} \tag{3.2}$$

where σ is the standard deviation of the kernel, and x and y are the horizontal and vertical differences from the central pixel of the kernel, respectively. Let $*$ denote the convolution operator, where the convolution C_{ij} between the image A_{ij} and the convolution matrix B with kernel size k is calculated as follows:

$$C_{ij} = B * A_{ij} = \begin{bmatrix} b_{11} & b_{12} & \dots & b_{k1} \\ b_{21} & b_{22} & \dots & b_{k2} \\ \vdots & \vdots & \ddots & \vdots \\ b_{k1} & b_{k2} & \dots & b_{kk} \end{bmatrix} * \begin{bmatrix} a_{[i-0.5k+0.5][j-0.5k+0.5]} & \cdots & a_{[i-0.5k+0.5][j+0.5k-0.5]} \\ a_{[i-0.5k+1.5][j-0.5k+0.5]} & \cdots & a_{[i-0.5k+1.5][j+0.5k-0.5]} \\ \vdots & \ddots & \vdots \\ a_{[i+0.5k-0.5][j-0.5k+0.5]} & \cdots & a_{[i+0.5k-0.5][j+0.5k-0.5]} \end{bmatrix}$$

$$= (b_{kk})(a_{[i-0.5k+0.5][j-0.5k+0.5]}) + (b_{k1})(a_{[i+0.5k-0.5][j-0.5k+0.5]}) + \cdots + (b_{11})(a_{[i-0.5k+0.5][j-0.5k+0.5]}) \tag{3.3}$$

For the case of the Gaussian convolution, the convolution matrix at pixel (i, j) in the image is defined as:

$$B_{xy} = \frac{1}{2\pi\sigma_{ij}^2} e^{-\frac{(x-0.5k-0.5)^2+(y-0.5k-0.5)^2}{2\sigma_{ij}^2}} \tag{3.4}$$

where σ_{ij} is the standard deviation of the image kernel A_{ij}, as show in Equation (3.3). In this algorithm, a gaussian convolution with $\sigma = 9$ and thus kernel of size 27, B_9 was applied to the

enhanced image I'_{ijt}. Let J_{ijt} represent the blurred image. As such,

$$J_{ijt} = B_9 * I'_{ijt} \tag{3.5}$$

3.2.5 Sobel Edge Detector

The Sobel operator applies the numerical approximation of the gradient and replaces the intensity J_{ijt} with the magnitude of its gradient, ∇J_{ijt}. There are two Sobel Operators, the X operator, G_x and the Y operator, G_y. In this algorithm, the X and Y operators were applied independently to the blurred image J_{ijt} to obtain the Sobel image K_{ijt}, with enhanced edges.

The X Sobel operator was approximated as:

$$G_x = \begin{bmatrix} 1 & 0 & -1 \\ 2 & 0 & -2 \\ 1 & 0 & -1 \end{bmatrix} \tag{3.6}$$

The Y Sobel operator was approximated as:

$$G_y = \begin{bmatrix} 1 & 2 & 1 \\ 0 & 0 & 0 \\ -1 & -2 & -1 \end{bmatrix} \tag{3.7}$$

The edge enhanced image K_{ijt} was thus calculated as:

$$K_{ijt} = \nabla J_{ijt} = \sqrt{(G_x * J_{ijt})^2 + (G_y * J_{ijt})^2} \tag{3.8}$$

where J_{ijt} is the blurred image, and K_{ijt} is the enhanced image. After processing, intensity enhancement (i.e. equation (3.1)) was applied, with $I_{min} = \bar{K}_{ijt}$ and $I_{max} = \bar{K}_{ijt} + 2\sigma$ so as to amplify the intensities of the edges.

3.2.6 Morphological Image Processing

In order to remove cellular artifacts, which are generally round in shape, morphological image opening (morphological erosion followed by dilation) and morphological image closing (morphological dilation followed by erosion) were applied sequentially to the image. The structural element was defined to be a rectangular kernel of size $51X7$ pixels. Erosion involves replacing the central pixel value with the minimum pixel value in the kernel, while dilation involves replacing the central pixel value with maximum pixel value in the kernel.

3.2.7 Algorithm to Extract Bounds of the Diameter

1. First order smoothing was applied to the intensity profile obtained from the morphologically processed image

2. The numerical first difference was then calculated of the aforementioned intensity profiles

3. Any relative maxima found above an empirically determined threshold, in this case the mean intensity, was then determined from the first difference.

4. The two maxima closest to the center of the vessels were then approximated as the bounds of the diameter, because the probability that high intensity artifacts exist in the interior of the blood vessel is low.

First order smoothing was performed, utilizing 10 points on either side of the pixel of interest. Let x_j denote the intensity of the pixel at position j for any arbitrary row. Utilizing the smoothing algorithm, x_j was smoothened as:

$$\bar{x}_j = \begin{cases} \frac{1}{10}\sum_{n=j}^{j+10} x_n & j < 10 \\ \frac{1}{10}\sum_{n=j-5}^{j+5} x_n & 10 \leq j \leq M-10 \\ \frac{1}{10}\sum_{n=j-10}^{j} x_n & j > M-10 \end{cases} \tag{3.9}$$

where M is the number of columns in the image and $\bar{x}_j$ is the smoothened intensity vector. The numerical first difference of order 4 relative to the columnar location of the pixel, j, was then calculated as follows:

$$\frac{\partial x_j}{\partial j} = x'_j = \begin{cases} -\frac{25}{12}x_j + 4x_{j+1} - 3x_{j+2} + \frac{4}{3}x_{j+3} - \frac{1}{3}x_{j+4} + O^4 & j < 2 \\ \frac{1}{12}x_{j-2} - \frac{2}{3}x_{j-1} + \frac{2}{3}x_{j+1} - \frac{1}{12}x_{j+2} + O^4 & 2 \leq j \leq M-2 \\ \frac{1}{2}x_{j-2} - 2x_{j-1} + \frac{3}{2}x_j + O^2 & j > M-2 \end{cases} \tag{3.10}$$

where M is the number of columns in the image. Because the intensities being analyzed are at pixel resolution, and sub-pixel resolutions are meaningless with respect to this form of analysis, advanced root finding techniques are not necessary to find the zeros of the first difference, which correspond with the intensity maxima. As such, a root was defined when either if the following criteria were satisfied:

1. $x'_j > 0$
2. $x'_{j+1} \leq 0$
3. $x_j > \bar{x}_j$

where $\bar{x}_j$ is the mean intensity. If all the following criteria were satisfied, then position j was found to be a root. These methods are summarized in **Figure 3.2**.

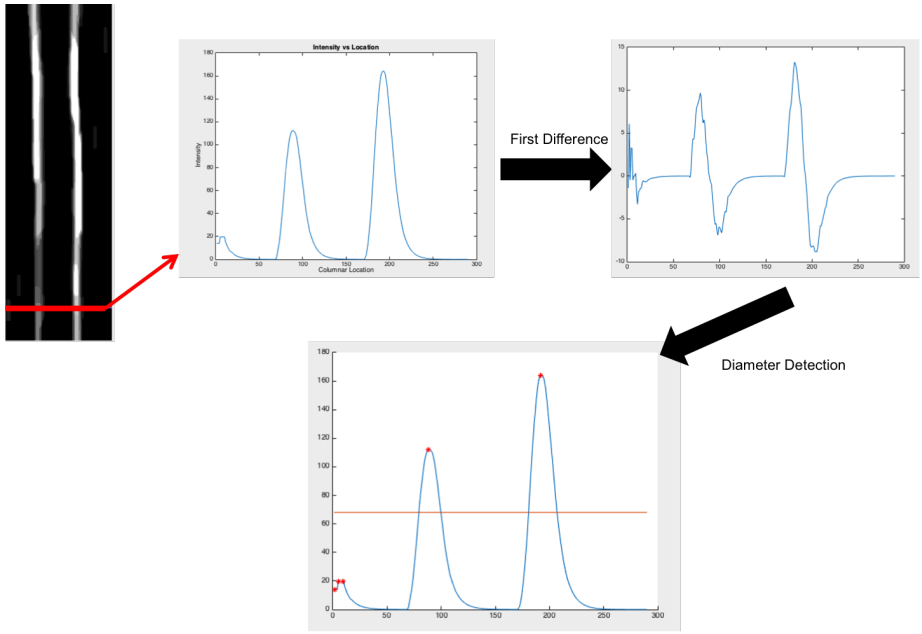

Figure 3.2: Summary of the Algorithm to Determine Diameter

3.2.8 Output Smoothing

Once the bounds were determined, the output of the vessel mapping algorithm was smoothened in order to avoid jumps when outlining the vessel boundary. Let l_{jt} represent the left pixel boundary and r_{jt} represent the right pixel boundary, for $j \in [0, M]$ and $t \in [0, T]$, where M is the number of rows and T is the number of columns. The following smoothing algorithm was performed on both l_{jt} and r_{jt}:

$$l_{jt} = \left(1 - \frac{|l_{jt} - l_{(j-1)t}|}{3 + |l_{jt} - l_{(j-1)t}|}\right) l_{jt} + \frac{1}{j}\left(\frac{|l_{jt} - l_{(j-1)t}|}{3 + |l_{jt} - l_{(j-1)t}|}\right) \sum_{n=0}^{j} l_{nt} \tag{3.11}$$

$$r_{jt} = \left(1 - \frac{|r_{jt} - r_{(j-1)t}|}{3 + |r_{jt} - r_{(j-1)t}|}\right) r_{jt} + \frac{1}{j}\left(\frac{|r_{jt} - r_{(j-1)t}|}{3 + |r_{jt} - r_{(j-1)t}|}\right) \sum_{n=0}^{j} r_{nt} \tag{3.12}$$

This algorithm was written in Java for implementation in ImageJ software (NIH, Bethesda, Maryland).

3.3 Results and Discussion

3.3.1 Evaluation of Image Processing

Following intensity enhancement and thresholding, a Guassian blur was utilized to smoothen the intensity profile. Implementation of the Gaussian blur ensured that the Sobel edge detector did not yield erroneous edges due to sudden changes intensity from random noise. These results are summarized in **Figure 3.3**.

The novelty of the algorithm employed here involves utilization of a custom morphological processing structural element designed to eliminate cellular artifacts. As shown in **Figure 3.4**, a rectangular morphological element was effectively able to eliminate cellular artifacts while preserving vessel boundary edge enhancement.

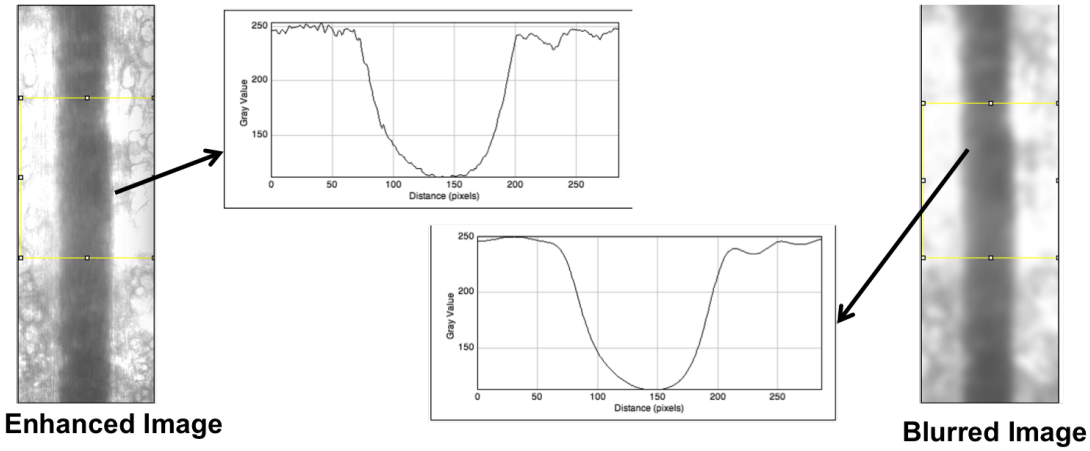

Figure 3.3: Effects of Gaussian Blur on Intensity Profile.

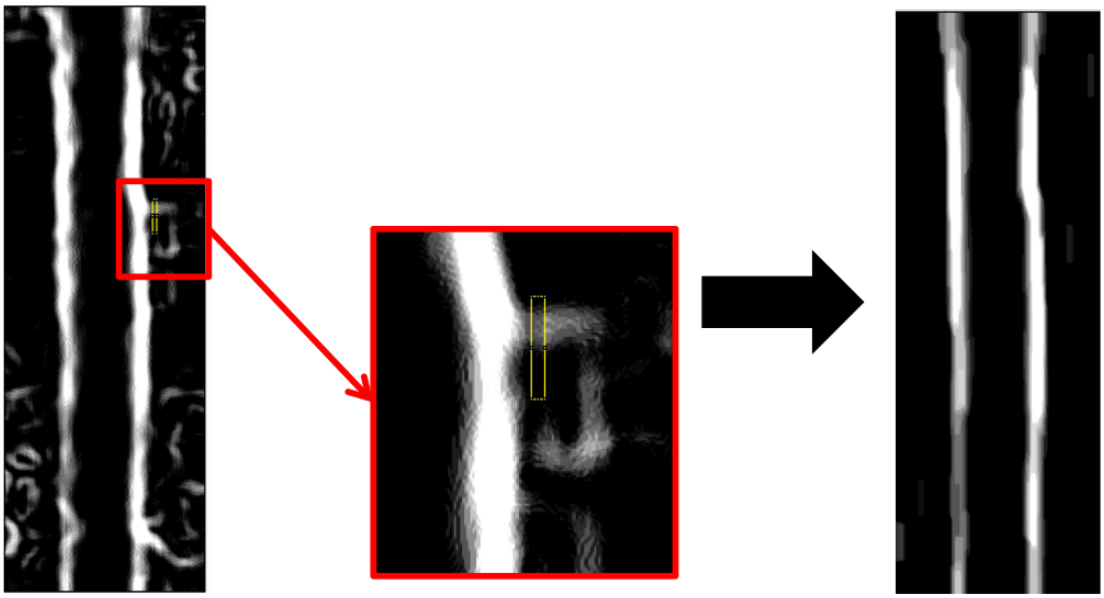

Figure 3.4: Morphological Processing Structural Element.

From the morphologically processed image, application of the algorithm detailed above was utilized to automatically extract the pixel distance of the diameter. Unlike other methods, this algorithm provides a numerical indication of the diameter of the vessel as a function of space. Consequently, the algorithm compressed multidimensional image information into a single one dimensional vector, encoding diameter.

3.3.2 Application of the Algorithm

Figure 3.5 shows application of the algorithm to two different videos from different animal models. From these figures, it clear that the algorithm is robust and accurate in outlining the diameter of the vessel for further application. Future directions would involve implementing this algorithm as a part of a neural network for a more accurate determination of vessel diameter.

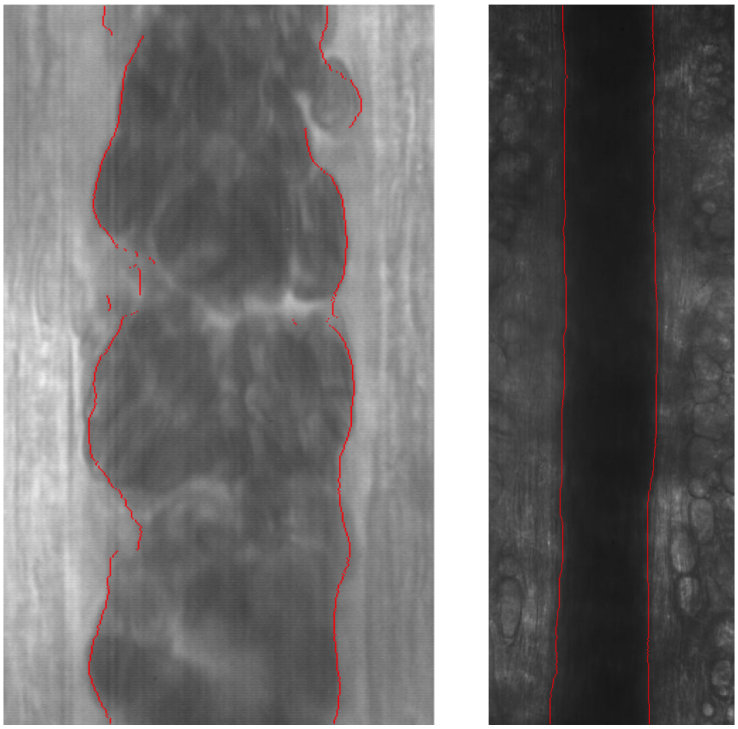

Figure 3.5: Application of the Diameter Detection Algorithm for **Left:** Detection of the Cell Free Layer in a Microvessel imaged from the rat cremaster muscle, and **Right:** Detection of the Diameter in a Microvessel imaged from the hamster dorsal skinfold window chamber. As demonstrated above, the algorithm was both robust and versatile in its ability to extract the diameter from the image.

3.4 Conclusion

The algorithm presented here presents improved computer vision and image processing techniques developed to analyze the spatial variations in the arteriolar cell free layer within a single vessel. Compared to other methods, which generally exploit binary thresholding via Otsu's method, the method presented here is more robust and less sensitive to variability in image acquisition. As demonstrated above, it is clear that the algorithm is robust and accurate in identifying the diameter of the vessel for further application regardless of animal model or imaging acquisition. Future directions would involve implementing this algorithm as a part of a neural network for a more accurate determination of vessel diameter.

Bibliography

[1] Y C Fung. Blood flow in the capillary bed. *Journal of Biomechanics*, 2(4):353–372, 1969.

[2] M Intaglietta. Hemodilution and Blood Substitutes. *Artificial Cells, Blood Substitutes, and Biotechnology*, 22(2):137–144, jan 1994.

[3] W David Strain and P M Paldánius. Diabetes, cardiovascular disease and the microcirculation. *Cardiovascular Diabetology*, 17(1):57, apr 2018.

[4] Nanae Hangai-Hoger, Parimala Nacharaju, Belur N Manjula, Pedro Cabrales, Amy G Tsai, Seetharama A Acharya, and Marcos Intaglietta. Microvascular effects following treatment with polyethylene glycol-albumin in lipopolysaccharide-induced endotoxemia. *Critical care medicine*, 34(1):108–117, 2006.

[5] Brian P Helmke, Shannon N Bremner, Benjamin W Zweifach, Richard Skalak, and Geert W Schmid-Schnbein. Mechanisms for increased blood flow resistance due to leukocytes. *American Journal of Physiology-Heart and Circulatory Physiology*, 273(6):H2884–H2890, 1997.

[6] A M Benis and J Lacoste. Distribution of blood flow in vascular beds: model study of geometrical, rheological and hydrodynamical effects. *Biorheology*, 5(2):147–161, 1968.

[7] Robin Fåhraeus. The suspension stability of the blood. *Physiological Reviews*, 9(2):241–274, 1929.

[8] Pedro Cabrales, Amy G Tsai, John A Frangos, and Marcos Intaglietta. Role of endothelial nitric oxide in microvascular oxygen delivery and consumption. *Free Radical Biology and Medicine*, 39(9):1229–1237, 2005.

[9] Sangho Kim, Peng Kai Ong, Ozlem Yalcin, Marcos Intaglietta, and Paul C Johnson. The cell-free layer in microvascular blood flow. *Biorheology*, 46(3):181–189, 2009.

[10] Ozlem Yalcin, Vivek P Jani, Paul C Johnson, and Pedro Cabrales. Implications Enzymatic Degradation of the Endothelial Glycocalyx on the Microvascular Hemodynamics and the Arteriolar Red Cell Free Layer of the Rat Cremaster Muscle. *Frontiers in Physiology*, 9:168, 2018.

[11] Marcos Intaglietta, Paul C Johnson, and Robert M Winslow. Microvascular and tissue oxygen distribution. *Cardiovascular Research*, 32(4):632–643, oct 1996.

[12] August Krogh. The number and distribution of capillaries in muscles with calculations of the oxygen pressure head necessary for supplying the tissue. *The Journal of Physiology*, 52(6):409–415, may 1919.

[13] Aleksander S Popel. THEORY OF OXYGEN TRANSPORT TO TISSUE. *Critical reviews in biomedical engineering*, 17(3):257–321, 1989.

[14] A M Y G TSAI, PAUL C JOHNSON, and MARCOS INTAGLIETTA. Oxygen Gradients in the Microcirculation. *Physiological Reviews*, 83(3):933–963, jul 2003.

[15] Claudia Scorcella, Elisa Damiani, Roberta Domizi, Silvia Pierantozzi, Stefania Tondi, Andrea Carsetti, Silvia Ciucani, Valentina Monaldi, Mara Rogani, Benedetto Marini, Erica Adrario, Rocco Romano, Can Ince, E Christiaan Boerma, and Abele Donati. MicroDAIMON study: Microcirculatory DAIly MONitoring in critically ill patients: a prospective observational study. *Annals of Intensive Care*, 8(1):64, 2018.

[16] Junfeng Zhang, Paul C Johnson, and Aleksander S Popel. Effects of Erythrocyte Deformability and Aggregation on the Cell Free Layer and Apparent Viscosity of Microscopic Blood Flows. *Microvascular research*, 77(3):265–272, may 2009.

[17] G R Cokelet and H L Goldsmith. Decreased hydrodynamic resistance in the two-phase flow of blood through small vertical tubes at low flow rates. *Circulation Research*, 68(1):1 LP – 17, jan 1991.

[18] W Reinke, P Gaehtgens, and P C Johnson. Blood viscosity in small tubes: effect of shear rate, aggregation, and sedimentation. *American Journal of Physiology-Heart and Circulatory Physiology*, 253(3):H540–H547, sep 1987.

[19] R H Adamson and G Clough. Plasma proteins modify the endothelial cell glycocalyx of frog mesenteric microvessels. *The Journal of Physiology*, 445(1):473–486, jan 1992.

[20] A R Pries, T W Secomb, and P Gaehtgens. The endothelial surface layer. *Pflügers Archiv*, 440(5):653–666, 2000.

[21] Merton Bernfield, Martin Götte, Pyong Woo Park, Ofer Reizes, Marilyn L Fitzgerald, John Lincecum, and Masahiro Zako. Functions of Cell Surface Heparan Sulfate Proteoglycans. *Annual Review of Biochemistry*, 68(1):729–777, jun 1999.

[22] Kurt Osterloh, Uwe Ewert, and Axel R Pries. Interaction of albumin with the endothelial cell surface. *American Journal of Physiology-Heart and Circulatory Physiology*, 283(1):H398–H405, jul 2002.

[23] Max Nieuwdorp, Marijn C Meuwese, Hans Vink, Joost B L Hoekstra, John J P Kastelein, and Erik S G Stroes. The endothelial glycocalyx: a potential barrier between health and vascular disease. *Current Opinion in Lipidology*, 16(5), 2005.

[24] Sheldon Weinbaum, John M Tarbell, and Edward R Damiano. The Structure and Function of the Endothelial Glycocalyx Layer. *Annual Review of Biomedical Engineering*, 9(1):121–167, jul 2007.

[25] Bernhard F Becker, Daniel Chappell, and Matthias Jacob. Endothelial glycocalyx and coronary vascular permeability: the fringe benefit. *Basic Research in Cardiology*, 105(6):687–701, 2010.

[26] National Research Council Committee US. Guide for the care and use of laboratory animals. Washington D.C.

[27] Silvio Baez. An open cremaster muscle preparation for the study of blood vessels by in vivo microscopy. *Microvascular Research*, 5(3):384–394, 1973.

[28] K I M SANGHO, KONG ROBERT L., POPEL ALEKSANDER S., INTAGLIETTA MARCOS, and JOHNSON PAUL C. A ComputerBased Method for Determination of the CellFree Layer Width in Microcirculation. *Microcirculation*, 13(3):199–207, jan 2010.

[29] Sangho Kim, Robert L Kong, Aleksander S Popel, Marcos Intaglietta, and Paul C Johnson. Temporal and spatial variations of cell-free layer width in arterioles. *American Journal of Physiology - Heart and Circulatory Physiology*, 293(3):H1526 LP – H1535, sep 2007.

[30] Pedro Cabrales, Beatriz Y Salazar Vázquez, Amy G Tsai, and Marcos Intaglietta. Microvascular and capillary perfusion following glycocalyx degradation. *Journal of Applied Physiology*, 102(6):2251–2259, jun 2007.

[31] Mathworks (2017). Matlab. Natick, MA. Available online at: https://www. mathworks.com/products/matlab.html.

[32] A R Pries, T W Secomb, P Gaehtgens, and J F Gross. Blood flow in microvascular networks. Experiments and simulation. *Circulation Research*, 67(4):826 LP – 834, oct 1990.

[33] Axel R Pries, Timothy W Secomb, Helfried Jacobs, Markus Sperandio, Kurt Osterloh, and Peter Gaehtgens. Microvascular blood flow resistance: role of endothelial surface layer. *American Journal of Physiology-Heart and Circulatory Physiology*, 273(5):H2272–H2279, nov 1997.

[34] David S Long, Michael L Smith, Axel R Pries, Klaus Ley, and Edward R Damiano. Microviscometry reveals reduced blood viscosity and altered shear rate and shear stress profiles in microvessels after hemodilution. *Proceedings of the National Academy of Sciences of the United States of America*, 101(27):10060 LP – 10065, jul 2004.

[35] T W Secomb, R Hsu, and A R Pries. A model for red blood cell motion in glycocalyx-lined capillaries. *American Journal of Physiology-Heart and Circulatory Physiology*, 274(3):H1016–H1022, mar 1998.

[36] Daniel Ortiz, Juan Carlos Briceño, and Pedro Cabrales. Microhemodynamic parameters quantification from intravital microscopy videos. *Physiological measurement*, 35(3):351, 2014.

[37] Sheldon Weinbaum, Xiaobing Zhang, Yuefeng Han, Hans Vink, and Stephen C Cowin. Mechanotransduction and flow across the endothelial glycocalyx. *Proceedings of the National Academy of Sciences*, 100(13):7988 LP – 7995, jun 2003.

[38] E R Damiano. Blood flow in microvessels lined with a poroelastic wall layer. *Poromechanics. J.-F. Thimus, Y. Abousleiman, AHD Cheng, O. Coussy, and E. Detournay, editors. Balkema, Rotterdam, The Netherlands*, pages 403–408, 1998.

[39] John M Tarbell and Zhong-Dong Shi. Effect of the glycocalyx layer on transmission of interstitial flow shear stress to embedded cells. *Biomechanics and Modeling in Mechanobiology*, 12(1):111–121, 2013.

[40] T W Secomb, R Hsu, and A R Pries. Effect of the endothelial surface layer on transmission of fluid shear stress to endothelial cells. *Biorheology*, 38(2, 3):143–150, 2001.

[41] M Jacob, M Rehm, M Loetsch, J O Paul, D Bruegger, U Welsch, P Conzen, and B F Becker. The Endothelial Glycocalyx Prefers Albumin for Evoking Shear Stress-Induced, Nitric Oxide-Mediated Coronary Dilatation. *Journal of Vascular Research*, 44(6):435–443, 2007.

[42] Mirella Gouverneur, Jos A E Spaan, Hans Pannekoek, Ruud D Fontijn, and Hans Vink. Fluid shear stress stimulates incorporation of hyaluronan into endothelial cell glycocalyx. *American Journal of Physiology-Heart and Circulatory Physiology*, 290(1):H458–H452, jan 2006.

[43] Jeffry A Florian, Jason R Kosky, Kristy Ainslie, Zhengyu Pang, Randal O Dull, and John M Tarbell. Heparan Sulfate Proteoglycan Is a Mechanosensor on Endothelial Cells. *Circulation Research*, 93(10):e136 LP – e142, nov 2003.

[44] J FENG and S WEINBAUM. Lubrication theory in highly compressible porous media: the mechanics of skiing, from red cells to humans. *Journal of Fluid Mechanics*, 422:281–317, 2000.

[45] Judith van Haare, M Eline Kooi, Jurgen W G E van Teeffelen, Hans Vink, Jos Slenter, Hanneke Cobelens, Gustav J Strijkers, Dennis Koehn, Mark J Post, and Marc van Bilsen. Metformin and sulodexide restore cardiac microvascular perfusion capacity in diet-induced obese rats. *Cardiovascular Diabetology*, 16(1):47, 2017.

[46] Hans Vink and Brian R Duling. Identification of Distinct Luminal Domains for Macromolecules, Erythrocytes, and Leukocytes Within Mammalian Capillaries. *Circulation Research*, 79(3):581 LP – 589, sep 1996.

[47] JOHN H Luft. Fine structures of capillary and endocapillary layer as revealed by ruthenium red. In *Federation proceedings*, volume 25, pages 1773–1783, 1966.

[48] Akinori Ueda, Manabu Shimomura, Mariko Ikeda, Ryuhei Yamaguchi, and Kazuo Tanishita. Effect of glycocalyx on shear-dependent albumin uptake in endothelial cells. *American Journal of Physiology-Heart and Circulatory Physiology*, 287(5):H2287–H2294, nov 2004.

[49] B Klitzman and B R Duling. Microvascular hematocrit and red cell flow in resting and contracting striated muscle. *American Journal of Physiology-Heart and Circulatory Physiology*, 237(4):H481–H490, oct 1979.

[50] Lujia Gao and Herbert H Lipowsky. Composition of the endothelial glycocalyx and its relation to its thickness and diffusion of small solutes. *Microvascular Research*, 80(3):394–401, 2010.

[51] Michael L Smith, David S Long, Edward R Damiano, and Klaus Ley. Near-Wall μ-PIV Reveals a Hydrodynamically Relevant Endothelial Surface Layer in Venules In Vivo. *Biophysical Journal*, 85(1):637–645, 2003.

[52] R T A Megens, S Reitsma, P H M Schiffers, R H P Hilgers, J G R De Mey, D W Slaaf, M G A oude Egbrink, and M.A.M.J. van Zandvoort. Two-Photon Microscopy of Vital Murine Elastic and Muscular Arteries. *Journal of Vascular Research*, 44(2):87–98, 2007.

[53] Bernard M van den Berg, Jos A E Spaan, and Hans Vink. Impaired glycocalyx barrier properties contribute to enhanced intimal low-density lipoprotein accumulation at the carotid artery bifurcation in mice. *Pflügers Archiv - European Journal of Physiology*, 457(6):1199–1206, 2009.

[54] S Reitsma, M G A oude Egbrink, H Vink, B M van den Berg, V Lima Passos, W Engels, D W Slaaf, and M.A.M.J. van Zandvoort. Endothelial Glycocalyx Structure in the Intact Carotid Artery: A Two-Photon Laser Scanning Microscopy Study. *Journal of Vascular Research*, 48(4):297–306, 2011.

[55] Eno E Ebong, Frank P Macaluso, David C Spray, and John M Tarbell. Imaging the Endothelial Glycocalyx In Vitro by Rapid Freezing/Freeze Substitution Transmission Electron Microscopy. *Arteriosclerosis, Thrombosis, and Vascular Biology*, 31(8):1908 LP – 1915, aug 2011.

[56] LAMKINKENNARD KATHLEEN A., JARON DOV, and BUERK DONALD G. Impact of the Fåhraeus Effect on NO and O2 Biotransport: A Computer Model. *Microcirculation*, 11(4):337–349, jan 2010.

[57] Yan Cheng Ng, Bumseok Namgung, and Sangho Kim. Two-dimensional transient model for prediction of arteriolar NO/O2 modulation by spatiotemporal variations in cell-free layer width. *Microvascular Research*, 97:88–97, 2015.

[58] P Mason McClatchey, Michal Schafer, Kendall S Hunter, and Jane E B Reusch. The endothelial glycocalyx promotes homogenous blood flow distribution within the microvasculature. *American Journal of Physiology-Heart and Circulatory Physiology*, 311(1):H168–H176, may 2016.

[59] HARRISON D G., WIDDER J., GRUMBACH I., CHEN W., WEBER M., and SEARLES C. Endothelial mechanotransduction, nitric oxide and vascular inflammation. *Journal of Internal Medicine*, 259(4):351–363, feb 2006.

[60] X. Yin and J. Zhang. Cell-free layer and wall shear stress variation in microvessels. *Biorheology*, 49(4):261–70, 2012.

[61] AR Pries, D Neuhaus, and P Gaehtgens. Blood viscosity in tube flow: dependence on diameter and hematocrit. *American Journal of Physiology-Heart and Circulatory Physiology*, 263(6):H1770–H1778, 1992.

[62] AR Pries. Blood viscosity in tube flow: dependence of diameter and hematocrit. *American Journal of Physiology*, 257:H1005–H1015, 1989.

[63] Travis Q Richardson and Arthur C Guyton. Effects of polycythemia and anemia on cardiac output and other circulatory factors. *American Journal of Physiology-Legacy Content*, 197(6):1167–1170, 1959.

[64] Pedro Cabrales, Amy G Tsai, and Marcos Intaglietta. Isovolemic exchange transfusion with increasing concentrations of low oxygen affinity hemoglobin solution limits oxygen delivery due to vasoconstriction. *American Journal of Physiology-Heart and Circulatory Physiology*, 295(5):H2212–H2218, 2008.

[65] Kang Li. The image stabilizer plugin for imagej, 2008.

[66] Nobuyuki Otsu. A threshold selection method from gray-level histograms. *IEEE transactions on systems, man, and cybernetics*, 9(1):62–66, 1979.

[67] Arthur C Guyton and Travis Q Richardson. Effect of hematocrit on venous return. *Circulation research*, 9(1):157–164, 1961.

[68] JW Crowell and EE Smith. Determinant of the optimal hematocrit. *Journal of Applied Physiology*, 22(3):501–504, 1967.

[69] James H Barbee and Giles R Cokelet. The fahraeus effect. *Microvascular research*, 3(1):6–16, 1971.

[70] Rachid Chebbi. Dynamics of blood flow: modeling of the fhruslindqvist effect. *Journal of biological physics*, 41(3):313–326, 2015.

[71] HERBERT H Lipowsky and JOHN C Firrell. Microvascular hemodynamics during systemic hemodilution and hemoconcentration. *American Journal of Physiology-Heart and Circulatory Physiology*, 250(6):H908–H922, 1986.

[72] F-Ch Fan, RY Chen, GB Schuessler, and S Chien. Effects of hematocrit variations on regional hemodynamics and oxygen transport in the dog. *American Journal of Physiology-Heart and Circulatory Physiology*, 238(4):H545–H522, 1980.

[73] STEVEN D House and HERBERT H Lipowsky. Microvascular hematocrit and red cell flux in rat cremaster muscle. *American Journal of Physiology-Heart and Circulatory Physiology*, 252(1):H211–H222, 1987.

[74] Tae H Han and James C Liao. Erythrocyte nitric oxide transport reduced by a submembrane cytoskeletal barrier. *Biochimica et Biophysica Acta (BBA)-General Subjects*, 1723(1-3):135–142, 2005.

[75] Xiaoping Liu, Alexandre Samouilov, Jack R Lancaster, and Jay L Zweier. Nitric oxide uptake by erythrocytes is primarily limited by extracellular diffusion not membrane resistance. *Journal of Biological Chemistry*, 277(29):26194–26199, 2002.

[76] John G Gibson, Alfred W Harris, and Verne W Swigert. Clinical studies of the blood volume. viii. macrocytic and hypochromic anemias due to chronic blood loss, hemolysis and miscellaneous causes, and polycythemia vera. *The Journal of clinical investigation*, 18(6):621–632, 1939.

[77] Ryan L Hoiland, Anthony R Bain, Mathew G Rieger, Damian M Bailey, and Philip N Ainslie. Hypoxemia, oxygen content, and the regulation of cerebral blood flow. *American Journal of Physiology-Regulatory, Integrative and Comparative Physiology*, 310(5):R398–R413, 2015.

[78] LE Allport, MW Parsons, KS Butcher, L MacGregor, PM Desmond, BM Tress, and SM Davis. Elevated hematocrit is associated with reduced reperfusion and tissue survival in acute stroke. *Neurology*, 65(9):1382–1387, 2005.

[79] Daniel Goldman, Ryon M Bateman, and Christopher G Ellis. Effect of decreased o2 supply on skeletal muscle oxygenation and o2 consumption during sepsis: role of heterogeneous capillary spacing and blood flow. *American Journal of Physiology-Heart and Circulatory Physiology*, 290(6):H2277–H2285, 2006.

[80] Bernhard Endrich, Kazuaki Asaishi, Alwin Götz, and Konrad Meßmer. Technical reporta new chamber technique for microvascular studies in unanesthetized hamsters. *Research in Experimental Medicine*, 177(2):125–134, 1980.